The Pennsylvania State University

The Graduate School

USING FIRST-PRINCIPLES CALCULATIONS AND MOLECULAR DYNAMICS TO INVESTIGATE THE PROPERTIES OF CESIUM-BASED HALIDE PEROVSKITES FOR PHOTOVOLTAIC APPLICATIONS

A Thesis in

Mechanical Engineering

by

Saeed Sameer Ibrahim Almishal

Submitted in Partial Fulfillment
of the Requirements
for the Degree of

Master of Science

May 2021

The thesis of Saeed Sameer Ibrahim Almishal was reviewed and approved by the following:

Ola Rashwan
Assistant Professor of Mechanical Engineering
Thesis Advisor

Brian Maicke
Associate Professor of Mechanical Engineering

Abdallah Ramini
Assistant Professor of Mechanical Engineering

Richard C. Ciocci
Associate Professor of Mechanical Engineering
Head of Graduate Program

ABSTRACT

Halide perovskites have gained tremendous research attention since the first solid-state perovskite solar cell in 2012 due to their optoelectronic properties and low processing temperatures. Most of the current research focuses on improving these perovskites' stability, tuning their bandgaps, and optimizing their optical properties. Finding a stable, non-toxic, environmentally friendly alternative to Pb^{+2} cation in halide perovskites compounds for photovoltaic applications has become critical due to the huge environmental concerns. Cesium-based halide perovskites have great potential as nontoxic alternatives for efficient solar cells with improved stability.

Computational materials simulations are needed to understand, study, and optimize their structures, stability, phase transformation, electronic and optical properties. In this thesis, the first-principles density functional theory (DFT) in VASP platform with two potential functionals PBE and PBEsol, were utilized to investigate the structural and electronic properties of $CsPbI_3$ polymorphs and the trigonal inorganic $CsGeI_{3-x}Br_x$ mixed-halide perovskites (x = 0.0, 1.0, 2.0 and 3.0) for photovoltaic applications.

Our results showed that for both $CsPbI_3$ and $CsGeI_{3-x}Br_x$, the bandgap edge states come mainly from B-X bonds. As the bromine content increases in $CsGeI_{3-x}Br_x$, the structural properties, such as the lattice parameters, Ge-X bond lengths, and volume, decrease. The bandgap calculations showed that the bandgap increased with the increase in the Br content. The electronic density of states revealed that only I 5p, Br 4p, and Ge 4s states contributed to the Valence Band Maximum (VBM) whereas, the Conduction Band Minimum (CBM) is mainly contributed by Ge 4p states in all compounds of $CsGeI_{3-x}Br_x$. Finally, a strong negative correlation was found between the Ge-X bond length and the bandgap.

Molecular dynamics in LAMMPS software package was also utilized to investigate the structural properties and phase transformation of $CsPbI_3$ by applying the appropriate force field. A

novel hybrid force field was introduced, referred to as “Hybrid EABC,” where EABC stands for Embedded-Atomic-Method and Buckingham- Coulomb potential. The outcomes from employing both Buckingham- Coulomb potential and Hybrid EABC were compared. The new Hybrid EABC potential succeeded in reproducing the experimentally reported and the ab initio structure’s radial distribution functions and phase transitions of $CsPbI_3$. Additionally, the novel Hybrid EABC molecular dynamics potential was able to detect the phase transformation from the orthorhombic to a cubic crystal structure and their melting temperatures at 594K and 750K, respectively, which agreed with the experimental values to within 1%. The new proposed hybrid potential proved to be accurate. It could potentially be used to infer the structure stability and the mechanical and thermal properties of the pure inorganic halide perovskites and the mixed halide perovskites which are used in various applications.

The main findings confirmed the high potential of the inorganic Ge-based mixed halide perovskites for the photovoltaic applications as non-toxic, environmentally friendly alternatives and provided insights into their stability, structural properties, and electronic properties.

Publication

The Molecular Dynamics Part of this work is published in RSC Advances; December 2020

Almishal, S. S., & Rashwan, O. (2020). New accurate molecular dynamics potential function to model the phase transformation of cesium lead triiodide perovskite ($CsPbI_3$). *RSC Advances, 10*(72), 44503-44511.

TABLE OF CONTENTS

LIST OF FIGURES

LIST OF TABLES

ACKNOWLEDGEMENTS

First of all, I would like to express my sincere gratitude to my advisor, Dr. Ola Rashwan, for all of her support, motivation, and advice throughout my graduate school career and the completion of my thesis. It was an honor to be under her guidance academically and personally. I am sure that this experience will have a great effect on my career and future.

I would like to thank Dr. Brian Maicke and Dr. Abdallah Ramini for serving on my M.Sc. committee and for their valuable comments and feedback. I would also like to thank Penn State Materials Research Institute (MRI) and Penn State Institutes of Energy and Environment (IEE) for supporting this work. Finally, I would like to thank the Pennsylvania State University's Institute for Computational and Data Sciences for their help and resources.

Finally, my deep and sincere gratitude to my family and friends for their continuous help and encouragement. I am forever indebted to my parents for their unparalleled love and support.

Chapter 1

Introduction

Halide perovskites are emerging as a new class of compelling materials for photovoltaic applications. These materials' performance surpassed all alternative technologies based on solution-processed materials in photovoltaic applications in a few years [1]. Although they only started with a power conversion efficiency of 3.8% in 2009 [2], a top device efficiency exceeding 25.2% has been recently reported [3]. Accordingly, Halide Perovskite Solar Cells, Halide PSCs, are among the fast-growing PV technologies ever known. Halide perovskites are synthesized with cheap and uncomplicated techniques due to their self-assembling characteristics, giving them an advantage over other demanding photovoltaic technologies, such as silicon-based solar cells. Additionally, metal halide perovskites are exceedingly appealing for photovoltaic applications due to their high absorption coefficient, high carrier mobility, tunable bandgaps, and low-temperature fabrication [4]-[9].

The building block of the halide perovskites is the ABX_3 perovskite structure, shown in Figure 1.1. This structure consists of a network of corner-sharing BX_6 octahedra, where the B atom is a divalent metal cation typically Pb^{2+}, Sn^{2+} or Ge^{2+} and X is a monovalent anion typically Cl^-, Br^-, or I^-. The A cation is selected to neutralize the total charge, and it could be an inorganics metal ion, such as Cs or Rb, or an organic molecule, such as Methylammonium or Formamidnium or a mix of both. The A cation must fit into the 12-fold location in the cubic phase. A tolerance factor is used to measure the deviation from the perfectly packed cubic perovskite structure. The desired structural and electronic properties can be engineered through a suitable choice of both the B and X elements forming the BX_6 octahedra and the A cation [10]- [14]. The choice of the A cation as

Cs^+ is the rational choice for stable perovskite solar cells with exceptional optoelectronic properties [15] - [20] .

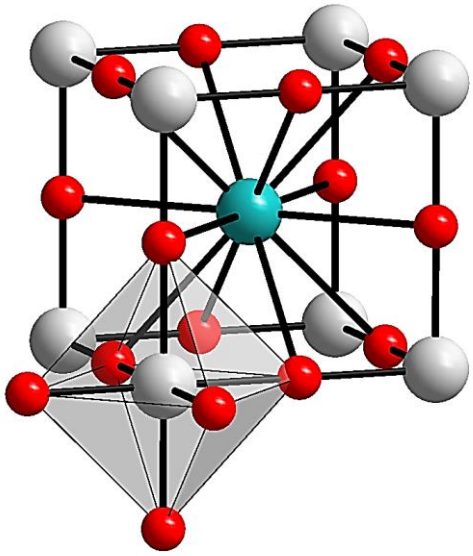

Figure 1-1: Perovskite crystal structure, the dark cyan ball represents cation A; white balls are lead or germanium, B; red balls represent halogen anions X.

Despite the substantial and swift progress in the perovskite-based solid-state photovoltaics, some of their functioning's key aspects are not yet totally understood. Understating the relationship between composition – structure – electronic properties is needed to speed up technological development and commercialization. In this work, we used computational methods, first-principles calculations, and molecular dynamics to investigate the structure, phase transformation, and electronic properties of Cs-based halide perovskites. The results achieved from this work give insight into the possibility of designing new functional structures with specific properties and enhanced performance.

Computational Background

Computational science has emerged as a powerful partner to experimental and theoretical studies. This section briefly introduces two levels of a materials system: the electronic structure level of nuclei and electrons and the atomistic or molecular level. The former's computational approach is the first-principles method, particularly density functional theory (DFT), and the computational approach of the latter is the molecular dynamics (MD). In this section, we introduce the most relevant equations and concepts that are used in the thesis. For a more elaborate introduction to DFT and MD, the readers are referred to the reference books [21]- [25].

Density Functional Theory (DFT)

Density Functional Theory (DFT) is a very effective technique for studying molecules and ions by directly solving an approximate version of the Schrodinger equation. The Schrodinger Equation, given in Equation 1.1 [21], describes the time-evolution of the wavefunction $\psi(\vec{r},t)$.

$$i\hbar\frac{\partial}{\partial t}\psi(\vec{r},t) = H\psi(\vec{r},t) \qquad 1.1$$

where the wavefunction $\psi(\vec{r},t)$ is complex-valued probability amplitude of finding a particle at a particular time, t, at the position, $\vec{r}$. H is the Hamiltonian operator, which is the quantum energy operator, and it is given in its most general form by equation 1.2 [21].

$$H = -\frac{\hbar^2}{2m}\left(\frac{\partial^2}{\partial x^2}+\frac{\partial^2}{\partial y^2}+\frac{\partial^2}{\partial z^2}\right)+U(\vec{r},t) = -\frac{\hbar^2}{2m}\nabla^2+U(\vec{r},t) \qquad 1.2$$

where $\hbar$ is the reduced Planck constant, m is the mass of the particle and $U(\vec{r},t)$ is the potential energy in the system.

The time-independent Schrodinger equation for the many-body wavefunction, Ψ, is given in Equation 1.3 [22] , which governs the wave function of a quantum-mechanical system and can be used effectively to define the material's properties.

$$H\Psi = E\Psi \tag{1.3}$$

where E is the eigenvalue and represents the total energy of the system. H, in this case, is given by relation 1.4 [22] and describes all of the quantum mechanical interactions between the nuclei, Nn, and the electrons, Ne, in the system.

$$H = -\sum_{i=1}^{Ne} \frac{\hbar^2}{2m} {\nabla_i}^2 - \sum_{i}^{Nn} \sum_{j}^{Ne} \frac{e^2 Z_i}{|\vec{r}_j - \vec{R}_i|} + \sum_{i<j}^{Nn} \frac{e^2 Z_i Z_j}{|\vec{R}_i - \vec{R}_j|} + \sum_{i<j}^{Ne} \frac{e^2}{|\vec{r}_i - \vec{r}_j|} \tag{1.4}$$

where $\vec{r_i}$ and $\vec{R_i}$ are the position vectors of the electron i and the nuclei i, respectively. Z_i is the atomic number of the nucleus i, and e is the electron charge.

The many-body time-independent Schrodinger equation is very complicated since it is a 3N dimensional function, where N is the number of electrons in the system. For instance, the complete specification of Si diamond unit cell with a discretization of 0.1 Å would require 10^{46} complex numbers.

Lots of approximations and attempts were introduced to closely solve the many-body time-independent Schrodinger equation, including the Hartree-Fock method [26]-[28]. All these approximations helped shape the fundamental ideas underlying the Density Functional Theory (DFT). Nevertheless, it was not until Hohenberg-Kohn theorem (1964) [29] and Kohn-Sham formulation (1965) [30] that the DFT was formally introduced. The core concept of DFT is that the ground state energy of the quantum system is a function of the electron density only n ($\vec{r}$) which is in turn is a function of three variables only. The electron density can be defined as the probability of finding an electron at position $\vec{r}$, and it is given by Equation 1.5 [22].

$$n(\vec{r}) = N \int \left|\Psi(\vec{r}, \vec{r}_2, \dots, \vec{r}_N; \vec{R}_1, \dots, \vec{R}_M)\right|^2 d\vec{r}_2 \dots d\vec{r}_N d\vec{R}_1 \dots d\vec{R}_M \quad 1.5$$

The Hohenberg-Kohn variational principle leads to Equation 1.6 [29].

$$\left[-\frac{1}{2}\nabla^2 + V_n(\vec{r}) + V_H(\vec{r}) + V_{xc}(\vec{r})\right]\phi_i(\vec{r}) = \varepsilon_i \phi_i(\vec{r}) \quad 1.6$$

where $\phi_i(\vec{r})$ is the individual wavefunction of the i[th] electron stemming from the independent electron approximation with ε_i as the corresponding eigenvalue. $-\frac{1}{2}\nabla^2$ is the kinetic energy of the electrons, $V_n(\vec{r})$ is the external nuclear potential, $V_H(\vec{r})$ is the Hartree potential, which satisfies the Poisson's equation as given by Equation 1.7 and $V_{xc}(\vec{r})$ is the exchange and correlation-function and is given by Equation 1.8 [22], [29].

$$\nabla^2 V_H(\vec{r}) = -4\pi\, n(\vec{r}) \quad 1.7$$

$$V_{xc}(\vec{r}) = \frac{\delta E_{xc}[n]}{\delta n}(r) \quad 1.8$$

E_{xc} is the exchange-correlation energy, and it represents what was not accounted for in the DFT theory. There is no full analytical representation available for this energy term. The research milestones in the DFT in the last decades is aimed to construct accurate approximations to $E_{xc}[n]$ and develop efficient algorithms for practical calculations. The local density approximation (LDA) is one of the simplest methods to construct $E_{xc}[n]$ by transforming any complex system into many pieces of uniform electron density with different values. Then, all energy terms can be identified by quantum Monte Carlo simulations [31], [32]. The generalized gradient approximation (GGA), in principle, should return better results than LDA as it includes both the electron density and its gradient at a given point [33], [34]. The exchange-correlation energy functionals used in this work are PBE [35] and PBEsol [36], which are simplified and improved GGA versions. These are further discussed in Chapter3 (Methodology).

Figure 1-2 shows a schematic flowchart for finding the self-consistent solutions of the Kohn-Sham equations. While conceptually it makes sense to compare densities to check for self-

consistency, in practical calculations, it is often more convenient to compare the total energies evaluated at two successive iterations.

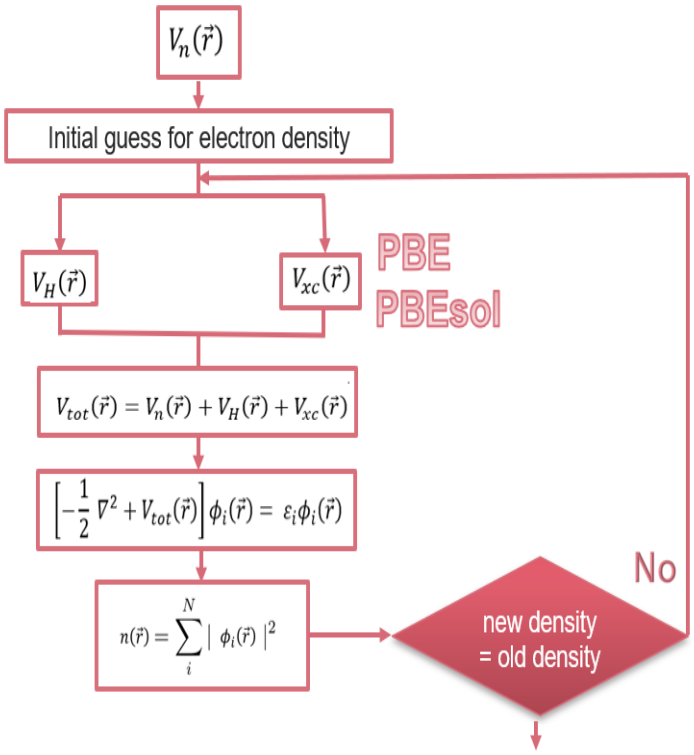

Figure 1-2: Schematic flow-chart for finding self-consistent solutions of the Kohn-Sham equations. We use PBE and PBEsol as our functionals in this work. This Figure is inspired by [22]

The atomic forces are calculated from the electron density and the total energy using the Hellmann-Feynman theorem to find a given structure's equilibrium configuration [37], [38]. Hellmann-Feynman forces are given by Equation 1.9. Following that, the nuclear position can be updated using the Verlet integrator [39].

$$F_I = Z_I\left[\int d\vec{r}\; n(\vec{r})\,\frac{\vec{r} - \overrightarrow{R_I}}{\left|\vec{r} - \overrightarrow{R_I}\right|^3} - \sum_{J\neq I} Z_J\,\frac{\overrightarrow{R_J} - \overrightarrow{R_I}}{\left|\overrightarrow{R_J} - \overrightarrow{R_I}\right|^3}\right] \qquad 1.9$$

Once the crystal equilibrium configuration is reached, it can be used to calculate the lattice parameters, volume, and bond lengths. The solutions of Kohn-Sham equations in a crystal are needed to obtain the electronic properties, including the projected density of states and the band structures. These are obtained using the crystal version of the Kohn-Sham equations given in Equations 1.10 and 1.11 [22].

$$\widehat{H_{\boldsymbol{K}}} u_{i\boldsymbol{K}} = \varepsilon_{i\boldsymbol{K}} u_{i\boldsymbol{K}} \tag{1.10}$$

$$\widehat{H_{\boldsymbol{K}}} = -\frac{1}{2}(\nabla + i\boldsymbol{K})^2 + V_{tot} \tag{1.11}$$

where $u_{i\boldsymbol{K}}$ is the periodic part of the eigenfunction that arises from the Bloch theorem [40], **K** is the wavevector, $\widehat{H_{\boldsymbol{K}}}$ is the modified Hamiltonian operator, and V_{tot} is all potentials in the system other than the kinetic potential.

The electron density $n(\vec{r})$ can now be calculated from Equation 1.12 [22], [24], [25].

$$n(\vec{r}) = \sum_i \int_{BZ} \frac{d\boldsymbol{K}}{\Omega_{BZ}} f_{i\boldsymbol{K}} |u_{i\boldsymbol{K}}(\vec{r})|^2 \tag{1.12}$$

where BZ is the Brillouin Zone, which is a uniquely defined primitive cell in reciprocal space, and Ω_{BZ} is the volume of the Brillouin Zone. $f_{i\boldsymbol{K}}$ is the occupation number of the eigenstate.

The density of electron states, $\rho(E)$, in dE quantifies how many Kohn-Sham states exist in the energy interval between E and E+dE. The density of electron states is defined by Equation 1.13 [22], [24], [25].

$$\rho(E) = \sum_i \int_{BZ} \frac{d\boldsymbol{K}}{\Omega_{BZ}} \delta(E - \varepsilon_{i\boldsymbol{K}}) \tag{1.13}$$

The band structure is generated by sweeping the wavevector **K** across the Brillouin zone and determining the corresponding eigenvalues $\varepsilon_{i\boldsymbol{K}}$, (i = 1, 2, 3 …). This step is a non-self-consistent calculation. It is typical to generate line plots with **K** varying along a K-path inside the Brillouin zone. For instance, to describe how the energy $\varepsilon_i(\boldsymbol{K})$ of the band i changes when **K** sweeps the segment between **K1** and **K2** is given by Equation 1.14 [22].

$$E_{i\boldsymbol{K}}(\kappa) = \varepsilon_i[\boldsymbol{K_1} + \kappa\,(\boldsymbol{K_2} - \boldsymbol{K_1})]\,, \qquad \kappa \in [0,1] \tag{1.14}$$

Classical Molecular Dynamics (CMD)

Classical Molecular Dynamics (CMD) is based on treating the atomic movement classically using Newton's laws. The classical treatment of atoms is achieved by approximating the atoms as solid spheres and averaging the electrons' presence. The general algorithm of the CMD simulation is illustrated in Figure 1-3 [23]. The algorithm begins with the initial conditions of position and velocity of all atoms at time zero. Then, force is calculated from the potential function. A new set of positions and velocities are then calculated using Newton's equations of motion [23], [41].

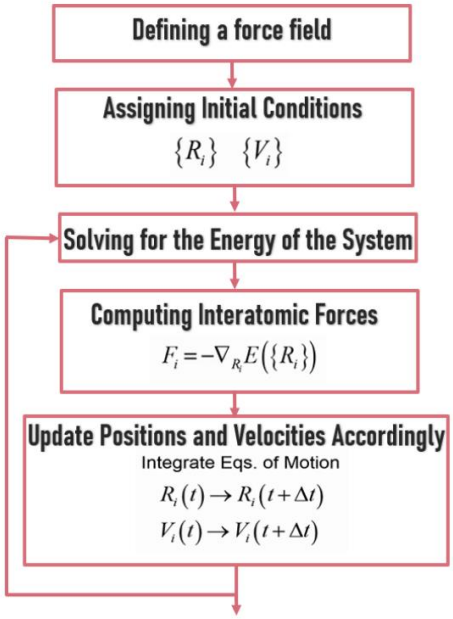

Figure 1-3: Schematic flow-chart for Equilibration of the structure using Molecular Dynamics. This figure is inspired by [23].

The total atomic force on each atom i, $\overrightarrow{F_i}$, is calculated from the gradient of the interatomic potential function, V, with respect to the atomic positions, $\overrightarrow{R_i}$ as illustrated in Equation 1.15 [23], [41].

$$\overrightarrow{F_i} = -\overrightarrow{\nabla_{R_i}}\, V(\{\overrightarrow{R_i}\}) \qquad 1.15$$

The classical Hamiltonian is defined in Equation 1.16.

$$H\left(\{\vec{R_i}\},\{\vec{P_i}\}\right) = \sum_{i=1}^{N} \frac{\vec{P_i}(t)^2}{2m_i} + V(\{\vec{R_i}\}) \quad 1.16$$

where m_i and $\vec{P_i}$ are the mass and momentum of atom i, respectively.

Advancing the atoms to the lower energy states through small time steps is achieved by solving the equations of motion presented in Equations 1.17 and 1.18 [23], [41].

$$\dot{\vec{R_i}} = {}^{\partial H}/_{\partial P_i} \quad 1.17$$

$$\dot{\vec{P_i}} = -{}^{\partial H}/_{\partial R_i} \quad 1.18$$

where $\dot{\vec{R_i}}$ and $\dot{\vec{P_i}}$ are the rate of change of position and momentum, respectively.

The finite difference method is used to solve the equations of motion in a step-by-step fashion. The Euler method is the fastest, but it is the least accurate because it is just a first-order integration scheme. Verlet algorithm offers an acceptable, reliable method to update the position every Δt interval as given in Equations 1.19. The time symmetry inherent in the Verlet algorithm reduces the level of local errors introduced into the discrete integration by removing all odd-degree terms. However, it is not a self-starting equation, so the position of the first-time step is found from Taylor's expansion of position as a function of t [23].

$$\vec{R_i}(t+\Delta t) = 2\vec{R_i}(t) - \vec{R_i}(t-\Delta t) + \ddot{\vec{R_i}}\,\Delta t^2 + O(\Delta t^4) \quad 1.19$$

The Velocity Verlet method, shown in Equation 1.20, is a stable method of velocity integration. In this method, velocity is updated every time step after both position and force have already been calculated [39].

$$\dot{\vec{R_i}}(t+\Delta t) = \dot{\vec{R_i}}\left(t+\frac{\Delta t}{2}\right) + \frac{\ddot{\vec{R_i}}(t+\Delta t)}{2}\Delta t \quad where\ \dot{\vec{R_i}}\left(t+\frac{\Delta t}{2}\right) = \dot{\vec{R_i}}(t) + \frac{\ddot{\vec{R_i}}(t)}{2}\Delta t \quad 1.20$$

Molecular Dynamics Potential Functions

When the forces used in the CMD simulation are calculated directly from quantum mechanical methods, the simulation is called Ab initio molecular dynamics, which was first introduced by Car and Parrinello in 1985 [42]. However, in classical molecular dynamics, the interatomic potentials are employed for a less computationally intensive approach. Lennard-Jones and Buckingham are typical examples of these potentials. These are obtained by fitting specific functions with quantum mechanical parameters, electronic structure calculations, or empirical methods. Because they are not fitted to the static properties, CMD potential functions are not transferable [23].

The interaction between the atoms can be categorized as bonded or nonbonded interactions. The bonded interactions model the bond behavior, including stretching, bending, and torsion [43]. The nonbonded terms are not chemical bonds, and they present the electrostatic and Van der-Walls interactions [41]. The system's total energy can then be represented as the sum of all interactions between all the atoms as distinct pairs, triplets, quadruplets, and so forth, as illustrated in Equation 1.21 [23].

$$E_{total} = \sum_{i<j}^{N} E_{2}\left(r_i, r_j\right) + \sum_{i<j<k}^{N} E_{3}\left(r_i, r_j, r_k\right) + \cdots \qquad 1.21$$

Figure 1-4 shows the schematic of the main two types of potential function representations used in this study: Interatomic pair potential and Embedded Atomic Method Potential.

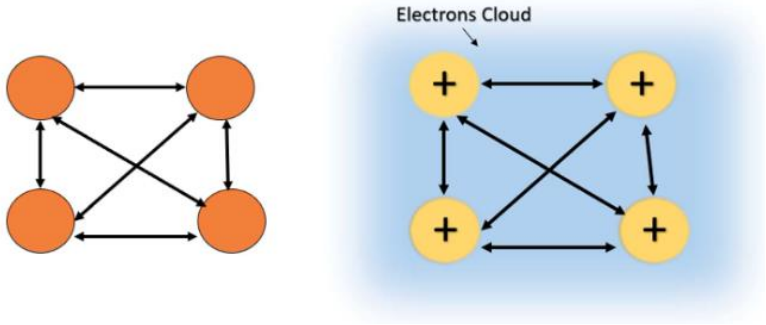

Figure 1-4: Representation of Pair Potential (Right) and Embedded Atomic Method Potential (Left) [44]

Interatomic pair potentials, as their name implies, neglect all the terms higher than the pair interaction in Equation 1.21 including interactions of triplets, quadruplets, and so forth. One of the most common pair potentials is Lennard-Jones potential, LJ, which was developed in 1924 for gases and spherical molecules [45] and is commonly used to model the covalent and Vander Walls interactions. The two common representations of LJ are given in Equation 1.22 [23].

$$U_{LJ}(r) = 4\varepsilon\left[\left(\frac{\sigma}{r}\right)^{12} - \left(\frac{\sigma}{r}\right)^{6}\right] = \frac{A}{r^{12}} - \frac{B}{r^{6}} \qquad 1.22$$

where r is the interatomic distance and ε, σ, A, and B are the LJ potential parameters that vary based on the material.

In 1938, Buckingham proposed a theoretical improvement of the Lennard-Jones potential, and it is shown in Equation 1.23 [46].

$$U_B(r) = Ae^{-\frac{r}{\rho}} - \frac{C}{r^6} \qquad 1.23$$

where r is the interatomic distance and A, C and ρ are the Buckingham potential parameters. The proposed exponential part was developed analytically, and hence it is more stable than the r^{12} term in LJ. Nonetheless, the attractive term dominates the potential's behavior at the short-range interactions due to the nearly constant exponential repulsive term [47].

Multiple successful attempts to fit LJ potential with Buckingham potential were reported. However, these methods are rather indirect and involve parameters of the loose form of the Buckingham potential [48], [49].

Adding the long-term coulombic interaction to Equation 1.23 leads to Equation 1.24, known as Buckingham-Coulomb potential function

$$U_{BC}(r_{ij}) = A_{ij}e^{-\frac{r_{ij}}{\rho_{ij}}} - \frac{C_{ij}}{r_{ij}^6} + \frac{q_i q_j}{4\pi\varepsilon_o r_{ij}} \qquad 1.24$$

where q_i and q_j are the effective charges of atom i and j, respectively.

This potential was successfully used in studying inorganic molecules and ionic crystals [50]. This potential was used in this work to represent polar covalent bonds.

Although pair interatomic potentials are simple and adequately model the material behavior, they overestimate the vacancy formation energy and may lead to substantial errors in the defects' evaluation. Moreover, the pair interatomic potentials fail in predicting the metallic crystal structure o and in modeling the surface relaxation behavior. This is mainly due to the neglection of all the higher terms of Equation 1.21 [51].

The pair potential could be improved dramatically and still be applicable for a large system by adding the embedding energy term. The resulting potential is known as the embedded-atom method potential (EAM). The EAM was first developed in 1984 by Daw and Baskes to study the hydrogen embrittlement in metals [52]. The EAM overcomes the limitations of the pair potentials, so it could successfully model the cohesion, the defects, the surface relaxation, and the ground-state impurity energies [23], [51], [53]. Generally, it improves the potential performance dramatically, and still, it could be applied to large systems. The EAM potential (U_{EAM}) is estimated using equation 1.25, which combines the terms of Equation 1.24 of the pair interaction and the embedding energy as a function of the electron density given in Equation 1.25.

$$U_{EAM} = \frac{1}{2}\sum_{i\neq j} U_{ij}(r_{ij}) + \sum_i F_i(\bar{\rho}_\iota) \quad 1.25$$

$$\bar{\rho}_\iota = \sum_{i\neq j} \rho_j(r_{ij}) \quad 1.26$$

where $U_{ij}(r_{ij})$ is the pair atomic interactions. ρ_j is the electron density contribution of atom j and $\bar{\rho}_\iota$ is the average total contribution from all atoms to the electron density at the position of atom i. $F(\bar{\rho}_\iota)$ represents the many-body behavior and approximates the energy required to insert the ionic cores into the electron density [23], [51], [53].

One of the standard methods of constructing the EAM potential is calculating the difference between the generated cohesive energy and the Universal Binding Curve, U_{UBC}. The Universal Binding Curve is an empirical fit of data of metallic systems [53]. Limited EAM potentials were generated and reported in the literature for some alloy systems [23]. In this work, we adopt two EAM potentials for Cs and Pb and combine them in a hybrid potential with Buckingham-Coulomb, as discussed in Chapter 3: Methodology

Chapter 2

Literature Review and Problem Statement

Density Functional Theory (DFT) and Molecular Dynamics (MD) investigations have been used to shed light on the links between the structure, chemical composition, and electronic properties of halide perovskites. These powerful computational tools have offered the possibility of designing new operational structures with the desired characteristics for various applications, including photovoltaics. In this chapter, a review of Density Functional Theory (DFT) and Molecular Dynamics (MD) application in studying halide perovskites is presented, discussed, and supported where possible with experimental work.

Density Functional Theory Calculations of Halide Perovskites

Density Functional Theory (DFT) is a computational tool to investigate the electronic structure and optical properties of materials. The last ten years witnessed an unprecedented acceleration in employing DFT in studying halide perovskites. Nevertheless, some first-principles pioneer studies were reported as early as 1996. Papavassiliou [54] had analyzed the electronic structures of some halide perovskites, including methylammonium lead iodide (MAPI) and methylammonium lead bromide (MAPBr), using the band calculations by a semiempirical method and the first-principles approach based on the Hartree-Fock theory. Koutselas, Ducasse, and Papavassiliou [55] also used the Hartree-Fock calculations to study energy gaps and excitonic binding energies of 3D, 2D, 1D, and 0D semiconducting materials that have lead halide or tin halide units as their basic building blocks.

Umebayashi et al. [56] studied the effect of dimensionality on the electronic structures of 3D- MAPI structure and 2D -$(C_4H_9NH_3)_2PbI_4$ structure by the ultraviolet photoelectron spectroscopy and the first-principles band calculations. Their theoretical calculations were based on the self-consistent calculations of DFT with the generalized gradient approximation (GGA). Their work showed that the Valence Band Maxima (VBM) and the Conduction Band Minima (CBM) of MAPI and $(C_4H_9NH_3)_2PbI_4$ were composed primarily of the σ-antibonding states of the Pb 6s and I 5p orbitals and the σ-antibonding states of Pb 6p and I 5s orbitals, respectively. They also concluded bandwidth-narrowing and an increase in the bandgap energy with decreasing the dimensionality, which agreed with the previously reported results of [55].

The dynamic disorder of the MA cation and the temperature dependence of $MAPbX_3$ (X = Cl, Br, I) had been anticipated and investigated experimentally since the 1980s [57]. Accordingly, the organic halide perovskites $MAPbI_3$ or $MASnI_3$ solar cells are not stable under high temperature and humid conditions, which limits their commercialization [58]- [60]. Although the researchers have been investigating and trying to improve halide perovskites' stability, the root causes behind the loss of stability are not yet fully understood. Some research was geared towards replacing the MA^+ cation with the large metal cations, such as Cs^+ or Rb^+. Experimentally, the Cs ion has been employed to replace MA^+ to improve the long-term stability of solar cells [19], [20]. The $CsPbI_3$ inorganic PSCs were fabricated under open-air conditions with a power conversion efficiency of 4.13% [19]. Therefore, more research is still needed to improve its efficiency.

Chang et al. [61] used the first-principles pseudopotential total-energy calculations within the local density approximation (LDA) with (2 × 2 × 2) grid point sampling in the Brillouin zone to study the structural properties and electronic structure of $MAPbX_3$ and $CsPbX_3$. Their calculated lattice constants for the cubic structures were about 2% smaller than the experimental values reported in [57]. They concluded that the structural properties of $CsPbX_3$ resemble those of $MAPbX_3$. They showed that the lattice constants become larger while the elastic constants become

weaker, going from Cl to Br to I. They found a weak coupling of the organic molecule to the inorganic Pb-X chains with no severe electron orbitals overlap. This weak coupling could explain the small rotational energy barrier of the organic cation they examined and agreed with [57]. The band-edge states came mainly from the Pb-X chains in both $MAPbX_3$ and $CsPbX_3$ with direct bandgap. The VBM of $MAPbX_3$ was an antibonding state between Pb-s and X-p orbitals in the Pb-X chains, which agreed with the early results reported in [56]. The CBM was a non-bonding state between the Pb-p and the X-p orbitals.

Tin halide perovskites ($ASnX_3$) are another attractive subclass of halide perovskites where the lead cation is replaced by tin. Chiarella et al. [62] and Borriello et al. [63] used the QUANTUM-ESPRESSO package, while Chabot et al. [64] used Abinit code for GGA DFT calculations with a 4x4x4 Brillouin zone grid to study the role of the cation in the electronic structure and the nature of the optical transitions of tin halide perovskites. The MA cation plays an electron donor role in the tin halide perovskites [62] as it does in the lead halide perovskites [61]. For MASnBr3, it was found that the valence bands were dominated by the Br or Cl p orbitals contribution, while the conduction band was essentially dominated by the Sn p states, with a minor contribution from the Br p and Br d states or Cl p states [62]. Borriello et al. [63] studied the effect of the phase transition on the structural and electronic properties of $CsSnI_3$. They concluded that the two phase-transitions from the orthorhombic to tetragonal and from the tetragonal to cubic do not significantly affect the octahedron internal structure as the mean value of Sn-I bond lengths stayed almost the same but accompanied by a progressive decrease in the tilting of the octahedra. This might explain the decrease in bandgap going from the orthorhombic phase to the high-temperature cubic phase [63], [64]. The VBM of $CsSnI_3$ is mainly dominated by I p orbital contributions, whereas Sn p orbitals essentially dominate the CBM with a small contribution of I p orbitals. The high-temperature cubic phase of $CsSnCl_3$ shares the same trends in its electronic structure as $CsSnI_3$, but its lower temperature monoclinic phase has a wide-bandgap with dispersed bands along the z-direction due

to the breaking of the corner-sharing octahedra network [63]. Borriello et al. [63] also replaced the Cs in $CsSnI_3$ with formamidnium (FA) and MA. The largest bandgap was observed in $FASnI_3$, followed by $MASnI_3$ and $CsSnI_3$.

Germanium is another candidate for replacing lead in halide perovskites. Ge offers a solution to the toxicity of lead and introduces non-linear crystal structures for non-linear optical applications, such as laser frequency conversion. The room temperature phases of the $MAGeI_3$, FAGeI3, and $CsGeI_3$ are found experimentally to have a trigonal structure with R3m symmetry [13]. Tang et al. [65] used LDA DFT to study the electronic structure and linear optical properties of $CsGeI_3$. Their work revealed that the p orbitals from iodine and germanium contributed significantly to the CBM, while the VBM is dominated by the p orbital of iodine. In another study by the same group [66], they used DFT implemented in the CASTEP package to study the $CsGeX_3$. They found out that the optimized lattice angles of the $CsGeX_3$ were more distorted than the ones reported experimentally. The calculated band gaps decreased while the dielectric constant at zero frequency was increasing from $CsGeCl_3$ to $CsGeI_3$. Sa et al. [67] used VASP with the Perdew-Burke-Ernzerhof of (PBE) exchange-correlation function to study the effect of strain on the electronic properties of $MAGeX_3$. Their calculated bandgaps had the same decreasing trend of [66] going from I to Cl. They also showed that the bandgap decreased significantly with increasing the compressive strain. Lu et al. [68] compared the different $AGeX_3$ compounds where A is Cs, MA, FA, MO ($CH_3C(NH_2)_2^+$), and GA ($C(NH_2)_3^+$)). They carried their calculations by VASP with PBE DFT with 4x4x4 k-point sampling for structural optimization and 8x8x8 k-point sampling for optical and electronic properties. They found that the increase in Ge–X bonds (from Cl to I) in $MAGeX_3$ increased the volumes, weakened the covalent coupling of Ge–X, lowered the bandgaps, reduced the electron and hole effective masses, and red-shifted the absorption spectra, which greatly agree with the trends reported in [66], [67]. The VBM of $AGeI_3$ perovskites were mainly contributed by the I 5p and Ge 4s orbitals, whereas CBM were dominated by Ge 4p orbitals which

modified the original result found by [65]. In $AGeI_3$ perovskites, the bandgap increased, and the absorption spectrum blue-shifted in the sequence of Cs^+ / MA / FA / MO / GA. The $MAGeCl_3$ was found to be a hole transporting semiconductor, while $MAGeBr_3$ and $MAGeI_3$ demonstrated the ability of bipolar carrier transport. In the long-wavelength region of 450–800 nm, the absorption coefficient of $MAGeI_3$ was higher than that of $MAPbI_3$ [68].

In all previously mentioned studies [54] - [68], the structures consisted of a single metallic ion or an organic molecule (A), a single metal cation (B), and a single halide anion (X) in ABX_3. Though, halide perovskites can be mixed or doped. Indeed, the mixed perovskites offer a great platform to optimize structural stability and tune the halide perovskites' bandgap. The most common type studied extensively is the mixed-halide perovskite, where X can be I_xBr_{1-x} or $I_xCl_{1-x,}$ or Br_xCl_{1-x}. The mixed halide perovskites are found to improve the stability and quality of perovskite thin films, which could enhance the photoelectric performance [69] - [71].

Mosconi et al. [72] used the GGA- DFT implemented in QUANTUM-ESPRESSO to study the tetragonal phase of $MAPbI_2Br$ and $MAPbI_2Cl$, where they did an apical and an equatorial substitution. $MAPbI_2Br$ perovskite was found to show an increased bandgap compared to MAPI with 0.2 eV blue-shifted absorption, while $MAPbI_2Cl$ exhibited almost the same absorption onset as MAPI. Liashenko et al. [73] studied $CsPbBr_{3-x}Cl_x$. They used PBE- DFT implemented in QUANTUM-ESPRESSO with the K meshing of 4x4x4 for the orthorhombic phase, 8x8x8 mesh for cubic pure halide perovskites, and 5x5x5 mesh for the cubic mixed Br–Cl films. The positions for Cl and Br were randomly chosen to minimize the constant defect effect in the calculation. They showed that as Cl ions were substituted for Br ions, the bandgap increased nonlinearly.

The $CsPbI_{3-x}Br_x$ family has been widely investigated as they form a compromise between the appropriate and practical bandgap of $CsPbI_3$ and the relatively high stability of $CsPbBr_3$. The cubic phase of $CsPbI_2Br$ can exist at a lower temperature than $CsPbI_3$ and $CsPbBr_3$ with better structural stability [74]. Additionally, the DFT calculations showed that $MAPbI_{3-x}Br_x$ and $CsPbI_{3-}$

$_xBr_x$ have great potential for a stable ordered structure, particularly at x = 1, which manifests the occurrence of a specifically ordered arrangement of Br and I anions with minimized formation energy [75], [76]. $CsPbI_2Br$ perovskite films were fabricated with high quality at low temperatures [77], [78]. $CsPbI_2Br$ perovskite Solar cells with high stabilized efficiency of 14% were reported [79] - [81]. Using DFT via VASP, it was shown that by increasing the Br content in $CsPbI_{3-x}Br_x$, the non-perovskite structure's occurrence becomes more suppressed [82].

Metal cations can also be mixed and doped. Mosconi et al. [83] used DFT calculations to study $MAPb_xSn_{1-x}I_3$, where they concluded a decrease in the bandgap and shifting of the absorption onset to the near-IR with the increase in Sn content. Wang et al. [84] also used the DFT- based calculations to study $CsPb_xSn_{1-x}I_3$, and they noticed a bandgap reduction with the increase of Sn. Sinan et al. [85] set the halide composition to IBr_2 to investigate the mixed Sn-doped lead halide $CsPb_xSn_{1-x}IBr_2$ in the orthorhombic and cubic phases. They used PBE- DFT via VASP for their calculations with 4 × 4 × 2 k-point samplings. They found that the B−I bond lengths, lattice volumes, and bandgaps suffer a monotonic decrease with increasing the content of the Sn^{2+}ions. They concluded that the orthorhombic $CsPb_{0.75}Sn_{0.25}IBr_2$ and the cubic $CsPb_{0.25}Sn_{0.75}IBr_2$ have the most substantial absorption. Li et al. [86] had fabricated a series of $CsPb_xSn_{1-x}IBr_2$ and demonstrated that they had tunable bandgaps from 2.04 to 1.64 eV. They showed that $CsPb_xSn_{1-x}IBr_2$ have an improved power conversion efficiency of 11.53% with much-improved phase stability. Liang et al. successfully prepared $CsPb_{0.9}Sn_{0.1}IBr_2$ PCE, with a bandgap of 1.79 eV, in the ambient atmosphere without a glovebox which exhibited 11.3% power conversion efficiency [87].

Mayengbam et al. [88] partially replaced the Pb with Ge to study the cubic $MAGe_xPb_{(1-x)}I_3$. They performed PBE- DFT via ATK-VNL with 6 × 6 × 6 k sampling for the structural and electronic properties and with the 10 × 10 × 10 k mesh for the optical spectra and projected density of states (PDOS). The bandgap decreased with the increase of Ge as the CBM shifted downward while VBM stayed almost the same. Sun et al. [89] used DFT via VASP to study the tetragonal

$MAGe_xPb_{(1-x)}I_3$ perovskites. They noticed a narrowing in the bandgap with the increase in the Ge content within the mixed system. Still, the mixed system showed lower band gaps than the pure Pb- and Ge-based perovskites. From $AGeX_3$ materials studied by [68] and the $MAGe_xPb_{(1-x)}I_3$ studied by [88], $CsGeI_3$ was found to have the smallest bandgap while $MAGe_{0.875}Pb_{0.125}I_3$ had the most substantial absorption in the infrared region. For $CsPb_{1-x}Ge_xI_2Br$, Liang et al. [90] found a monotonic decrease in the bandgap with the increase in Ge using PBE via VASP. Yang et al. [91] succeeded in preparing $CsPb_{1-x}Ge_xI_2Br$ perovskites in an ambient atmosphere without a glovebox and reported a power conversion efficiency of 10.8 %. Without lead, $CsSn_{0.5}Ge_{0.5}I_3$ PSC was fabricated with a promising efficiency of up to 7.11% and very promising high stability [92].

Despite the substantial and tremendously fast progress in perovskite-based solid-state photovoltaics, some of the material aspects critical to their functioning, including stability, the origin of bandgaps, and optical absorption, are not yet totally understood. Although a large body of DFT calculations was reported for various halide perovskite materials, to the best of our knowledge, no structural or electronic calculations have been reported for the mixed halide $CsGeI_xBr_{1-x}$ systems in the trigonal phase. Additionally, there is no complete or consistent study investigating all three $CsPbI_3$ polymorphs with PBE or PBEsol functionals. Therefore, in this study, we employed PBE and PBEsol DFT via VASP to study the structural and electronic properties of $CsPbI_3$ polymorphs and the family of mixed $CsGeI_xBr_{1-x}$.

Molecular Dynamics Calculations of Halide Perovskites

Scientists and researchers have been trying to develop and test potential functions that can be used to evaluate stability and properly simulate perovskites' phase transition behavior. Oxide perovskites have been studied intensively. Particularly, $MgSiO_3$ for its abundance in the earth mantle [50]. Various potential functions representations were successfully used to study the oxide

perovskites including $MgSiO_3$, $BaTiO_3$, $CaTiO_3$ and $BaZrO_3$ [93] - [95]. In particular, Coulomb Buckingham potential stands out for its ease of application and stable numerical performance [50], [93], [94]. On the other hand, the literature lacks reliable potential functions to model halide perovskites. Still, halide perovskites share lots of their attributes with oxide perovskite, and the results of the oxide studies can be extended, modified, and enhanced to study halide perovskites [96], [12].

The first hybrid potential to model MA^+ based perovskites was developed by Mattoni et al. [96], [97], 'MYP,' by fitting on data from Ab initio models. In the MYP model, the inorganic-inorganic potential parameters were rescaled to Matusi $MgSiO_3$ parameters [50]. MA^+ ($CH_3NH_3^+$) was represented by the standard GAFF force field that includes bonded interactions. (Pb- I) and (C-N) interactions were modeled by Buckingham Coulomb-potential, while (H−Pb) and (H−N) interactions were modeled by Coulomb -LJ potential. They also assumed that the interaction between C−Pb is the same as N−Pb, and they both resemble Cs−Pb in $CsPbI_3$, and the same applies to C−I and N−I with respect to Cs−I. The MYP fitting parameters were further enhanced by refining the MA^+ atomic partial charges and Pb-I interactions to reproduce the density functional theory DFT calculations of the cohesive energy, Pb-I distortion energy, molecules reorientation energy, and bulk modulus of a hydrostatic deformed cubic crystal. Further, the N-I interaction was refined to ensure the orthorhombic-to-tetragonal transition [96], [97].

Mattoni et al. [96], [97] proved that the MYP calculations meet the experiments and DFT results on the critical structural and vibrational properties of the material, such as energy as a function of lattice spacing [96], [97]. In studying the phase transition, the potential produced the general features of the transition from the orthorhombic crystal structure to the tetragonal structure and to the cubic crystal structure. Nevertheless, MYP was also used to determine the sources of phase transition in $MAPbI_3$, mainly attributed to the dynamic behavior of organic cations in the

lead iodide lattice [98]. The MYP was further employed in studying the diffusion of point defects, and it showed that the dominant mechanism of ionic transport in $MAPbI_3$ is iodine diffusion [99].

For its acceptable accuracy, the MYP force field was used to study the behavior of different phases of $MAPbI_3$ under various conditions. It was used to model the nucleation and interfacial mismatch during the vapor deposition of $MAPbI_3$ on the TiO_2 substrate [100]. It was also used to study phonon scattering [101], carrier mobility [102], polaronic strain [103] and to characterize qualitatively the nature and the relaxation properties of the dielectric polarization [104]. The use of MYP was not limited to 3D structures. It was used to study the thermal conductivity of 2D $MAPbI_3$ thin films [105]. However, the resulted volume as a function of the temperature curve from the MYP has discrepancies compared to the experimental results because the model ignored the charge redistribution and the covalent nature of lead iodide interactions [96], [97].

Hata et al. [106] studied $MAPbBr_3$ using the same MYP potential used by Mattoni [97]. They used the same Pb−Pb, Pb−MA, and MA internal interactions as $MAPbI_3$. They calibrated the newly introduced parameters based on five scaling factors for developing a force-field for $MAPbBr_3$. Three are for scaling; namely: α for coulomb -Buckingham parameters, β for the charges and γ for organic-inorganic interactions. Two additional factors result from the dynamics of phase transition, which are A_{OI} and ρ_{OI} of Br− (C, N). Although the developed model is simple, it reproduces, to a certain extent, the main static, and thermodynamic properties of $MAPbBr_3$ [97], [106]. $MAPbBr_3$ has almost the same molecular dynamic behavior as $MAPbI_3$. However, the volume of $MAPbBr_3$ is consistently smaller than that of $MAPbI_3$. The change of volume-temperature curve slope for $MAPbBr_3$ is at 140−170 K compared to 150−200 K for $MAPbI_3$. This was attributed to orthorhombic-to-tetragonal phase transition in [97]. Moreover, the anisotropy in orthorhombic phase, longest to shortest lattice parameter ratio, of $MAPbBr_3$ is slightly higher than that of $MAPbI_3$ but still was underestimated relative to the experimental value. However, it is overestimated for $MAPbI_3$. For both $MAPbBr_3$ and $MAPbI_3$, the calculated anisotropy does not

change upon the phase transition from tetragonal to cubic, which can be understood from the limitations of the two-body potentials for inorganic lattices. Still, by calibrating mixed I−Br interactions, it would be possible to model the large class of mixed systems $MAPbI_xBr_{1-x}$ [106].

Molecular dynamics simulations were used to study the effect of moisture on $MAPI_3$, which is highly hydrophilic. An MYP-based force field (MYP1) for water–MAPI systems was developed to study the dissolution of $MAPbI_3$ crystals in water [107]. It was further used to clarify that the apparent hydrophobic experimental contact angle resulted from the surface degradation during measurement [108]. Despite the accuracy of the models developed by Mattoni et al. [96] and Hata et al. [106], these models cannot predict the complex crystal structure transitions, and they are not transferrable to mixed halides perovskites $MAPb(I_{1-x}Br_x)_3$.

Handley and Freeman [109] also presented a set of interatomic potentials for modeling $MAPbI_3$ that included short-range interactions for the lead and iodide interactions to improve the degree of transferability. Artificial intelligence algorithms, such as artificial neural networks (ANN) and Genetic algorithms (GA), were employed to develop force fields that could represent the mixed halide perovskites. Chen and Pao [110] used artificial neural networks (ANN) to model complex structures and transitions. They demonstrated that by developing an ANN potential for $MAPbI_3$ as an example. Marchenko et al. [111] developed a semi-empirical model representing the mixed halides hybrid perovskites and used it to calculate Gibbs free energy and thermodynamic properties.

Generally, molecules such as MA+ introduce complex dynamics because of the molecular orientations and hence molecular entropy. As has been established in the previous section, Cs can effectively replace MA. So various experimental and first principal studies have investigated $CsPbI_3$. Nevertheless, there is not yet enough research on the molecular dynamics of this structure [112], [113]. Balestra et al. [114] used genetic algorithms to adjust the Coulomb-Buckingham pair atomic potentials to model the mixed halide systems of $CsPb(I_xBr_{1-x})_3$. They used their modified

potential values to reproduce the DFT calculations of the lattice geometric distortions energies. However, their modified force field was fitted only to cubic structures of $CsPbI_3$, $CsPbBr_3$, and mixed $CsPbI_3Br$ to be transferable between them. The radial distribution function of the cubic $CsPbI_3$ was successfully obtained and matched the experimental results [114]. However, the new derived force field acceptably agreed with experiments and previous theoretical studies of structural and dynamic properties, particularly for the pure structures, i.e., the non-mixed, only in their cubic crystalline structure form.

Although the inorganic metal halide perovskites, particularly $CsPbI_3$, have unique properties and better stability than $MAPbI_3$, their structural properties and phase transitions are not well-characterized, and further investigation is needed. To the best of our knowledge, no potential function has been reported that can model the phase transformation of $CsPbI_3$ from the orthorhombic phase to the cubic one. Therefore, we introduce a novel hybrid force field referred to as "Hybrid EABC," where EABC stands for Embedded-Atomic-Method and Buckingham Coulomb potential. We compared the outcomes of using both Coulomb-Buckingham potential and Hybrid EABC in reproducing the experimentally reported and the ab initio structure's radial distribution functions and phase transitions of $CsPbI_3$.

Problem Statement and Research Questions

Based on the literature review, a research gap was found in studying the structure and the electronic behavior of the orthorhombic and cubic crystal structure of $CsPbI_3$ and the trigonal crystal structure of $CsGeI_{3-x}Br_x$. These crystal structures were proved experimentally to be the stable phase of these compounds in the solar cells' operating temperature range. Most studies in the literature assumed an ideal cubic crystal structure for its simplicity. Also, the properties and behavior of the Ge-based mixed halide perovskites needed in-depth investigation.

Therefore, the following research questions were formulated:

1. What is the type of band structure of the $CsGeI_{3-x}Br_x$ trigonal family?
2. How would the addition of EAM potential affect the accuracy and efficiency of modeling the phase transformation in $CsPbI_3$?
3. How does the replacement of Pb with Ge in $CsPbI_3$ affect the structural and electronic properties?
4. What effects does the increase in Br content have on the structural and electronic properties of $CsGeI_{3-x}Br_x$?
5. Does the substitution with Br increase or decrease the available density of states in the electronic structure?

Chapter 3

Methodology

Structural and Electronic Properties from Density Functional Theory Calculations

To investigate the structural and electronic properties of $CsPbI_3$ and $CsGeX_3$, we use density functional theory (DFT) using the Vienna ab initio simulation package, VASP [115], [116]. The accuracy and efficiency of the DFT calculations depend on the exchange-correlation functional choice, the pseudopotential, and the basis set for KS orbitals. VASP uses Projected-augmented wave (PAW) potential as its pseudopotential with plane waves as its basis set [115], [116]. PAW compromises between the efficiency of the pseudopotential and the accuracy of the all-electron potential [116].

For the exchange-correlation functional choice, discuss the commonly used PBE [35] and its variation PBEsol [36] functional. The original PBE functional has three parameters: μ, β and κ [35]. μ, appears in the exchange functional and was obtained from predicting the correct linear response of bulk Jellium using the combined exchange and correlation functional. β emerged in the correlation functions and was obtained in the original PBE functional by recovering the second-order gradient expansion of the correlation energy for weakly inhomogeneous high-density systems. κ comes from the Lieb-Oxford (LO) bound [117]. Consequently, in PBE, $\mu = \pi^2\beta/3$ which fixes μ given β. On the other hand, In PBEsol, μ is obtained by recovering the second-order gradient expansion of the exchange functional while β is fitted to Jellium surface energies (JSEs) [36], [118]. Therefore, PBEsol is biased towards solids and supposedly yields better equilibrium properties of densely packed solids due to its diminished gradient dependence [119]. Pedroza et al.

argue that although PBEsol has been constructed specifically for solids, it is not always the best functional for solids [120].

Both PBE and PBEsol are nonempirical approaches, which means they mainly rely on the exact functional's mathematical properties in maximizing the transferability of the proposed approximation for different properties and systems [119]. They also demonstrated that they generally work well in predicting structural properties within a 1%-3% error [23]. PBEsol was found to provide the lattice parameters closest to silicon experimental results and various insulators, including ZrSiO4 [121]. Other materials like carbon, Ca, Ba, Na, Al, LiF, and Fe2TiSn, PBE produced better structural results than PBEsol [122], [123]. Accordingly, we have used and compared using PBE [35] and PBEsol [36] functionals to study the structural properties of the materials studied in this work. All structures were relaxed until the forces on individual atoms are less than 0.001 eV/Å with a k-point sampling of 6x6x6, cutoff energy of 520 eV, and the accurate precision mode employed in VASP. The results of this step are the lattice parameters, volume, and bond lengths.

Although the electronic properties obtained with PBEsol are usually close to the ones obtained from PBE, PBEsol constantly underestimates the bandgap predicted by PBE [124]. This trend can be explained by the reduction in the μ parameter that leads to a reduction of the exchange contribution to the energy [124]. Because PBE is a great compromise between the computational demands and accuracy of the electronic properties results [125], we have carried the electronic properties calculations using only PBE. For the accurately projected density of states (PDOS) and band structure calculations, a denser k-point sampling mesh of 18x18x18 has been employed with a 10^{-8} eV electronic convergence criterion. An additional support grid for the evaluation of the augmentation charges was employed. The tetrahedron method with Blöchl corrections [126] was used for smearing with a width of 0.05 eV for PDOS calculations, while Gaussian smearing [127] was used in the band structures calculations. The bandgap can then be calculated from the band

structure. The atom and orbital projected density of states, the type of the band structure, whether direct or indirect and the bandgap are directly related to the studied structures' photovoltaic performance. The crystal structures have been visualized with VESTA [128] , and electronic properties were post-processed with VASPKIT [129] and MATLAB.

Phase transformation of $CsPbI_3$ by Molecular Dynamics

The molecular dynamic simulator used in this study is the Linear atomic/molecular massive parallel simulator LAMMPS [130]. Molecular Dynamics Simulations require two main inputs. First, atoms' initial positions, which we obtained from our DFT calculations discussed in the previous section. Secondly, the force field. We discuss and test the application of two force fields that we developed to model $CsPbI_3$ structural properties at ambient conditions and phase transformation. The first force field follows the Buckingham-Coulomb representation, which is an interatomic pair potential. The second force field is Hybrid EABC, which is based on applying interatomic pair potentials combined with the Embedded Atomic Method (EAM).

Buckingham- Coulomb Pair Potential

We used Buckingham-Coulomb potential (U_{BC}) to model the pair atomic interactions due to the inorganic nature of $CsPbI_3$ bonds. This potential is used effectively in studying inorganic and ionic crystals [50]. The general schematic of Buckingham-Coulomb interactions was shown in Figure 1-4. In Buckingham-Coulomb potential (U_{BC}), long-term coulomb interaction is added to Buckingham potential, as shown in Equation 1.24 and repeated here for completeness.

$$U_{BC}(r_{ij}) = A_{ij}e^{-\frac{r_{ij}}{\rho_{ij}}} - \frac{C_{ij}}{r_{ij}^6} + \frac{q_i q_j}{4\pi\varepsilon_o r_{ij}} \qquad (1.24)$$

where r_{ij} is the distance between atoms i and j, q_i and q_j are their respective effective charges, and A_{ij}, ρ_{ij} and C_{ij} are the Buckingham potential parameters of the pair atoms i and j [46].

The potential parameters for the six interactions are required to completely define the force field between the constituent ions of $CsPbI_3$ perovskite. For the parameters of Cs-Cs and Cs-I Interactions, the Buckingham parameters were obtained from Sangster and Atwood [131]. Mirskaya proposed a numerical technique based on the geometric mean combining rule for the total interaction energy of two non-bonded atoms for the Buckingham Potential [132]. Therefore, we used the Mirskaya technique for Cs-Pb, interaction. Equations 4 and 5 show the Mirskaya technique tailored to our case.

$$A_{Cs-Pb} = \sqrt{A_{Cs-Cs} \times A_{Pb-Pb}} \qquad 3.1$$

$$\rho_{Cs-Pb} = \frac{2\rho_{Cs-Cs} \times \rho_{Pb-Pb}}{\rho_{Cs-Cs} + \rho_{Pb-Pb}} \qquad 3.2$$

For $C_{Cs\text{-}Pb}$, an iterative algorithm was developed to find the ideal value. This value was approximately the same value for $C_{Cs\text{-}Pb}$ obtained by Mirskaya [132] method when applied to the $C_{Cs\text{-}Cs}$ and $C_{Pb\text{-}Pb}$ evaluated by Balestra et al. [114].

For Pb-Pb, Pb-I, and I-I interactions parameters, they were set to be equal to the ones in MYP [96]. The effective charge of Cs^+ was assumed to be the same charge of MA^+ as in $MAPbI_3$ [96], [97]. These interactions, along with the effective charges, are summarized in Table 3-1.

Table 3-1: Coulomb Buckingham Potential Model Parameters of $CsPbI_3$ [44]

Interaction	$A\ (eV)$	$\rho\ (\dot{A})$	$C\ (eV\dot{A}^6)$	*Ion*	*Effective Charge*
Cs-Cs	3.584x1016	0.0843	240.34		
Cs-Pb	3.3068x1011	0.10519	480.0	Cs	1.36
Cs-I	4913.000	0.3814	480.06		
Pb-Pb	3051120.5	0.131258	0.0	Pb	2.03
Pb-I	4488.05	0.321737	0.0		
I-I	988.42	0.482217	30.22285	I	-1.13

Molecular Dynamics Hybrid EABC Potential

Although pair interatomic potentials are simple and adequately model the material behavior, they do not reflect bonds' true nature. They overestimate the vacancy formation and fail to predict metals' crystal structure and model surface relaxation behavior [51]. This is expected as all the higher terms of atomic interactions other than pair interactions are neglected [51], [23].

Therefore, in this work, we developed a new potential of $CsPbI_3$ by superimposing the Embedded Atomic Method (EAM) to BC pair potential to model both Cs-Cs and Pb-Pb interactions to reflect the metallic nature of these bonds. The EAM potential was first developed in 1984 by Daw and Baskes to study the hydrogen embrittlement in metals [52]. EAM potential (U_{EAM}) adds the embedding energy, representing the energy required to embed positively charged atomic cores into the electron density, to the pair atomic potential.

The EAM potential overcomes the limitations of pair potentials so it can successfully model the cohesion, defects, surface relaxation, and ground-state impurity energies [23], [51], [53].

Generally, it improves the potential performance dramatically and still applies to large systems computations. The EAM potential (U_{EAM}) is estimated using Equation 4 terms of pair interaction and embedding energy as a function of electron density given in Equation 5.

$$U_{EAM} = \frac{1}{2}\sum_{i\neq j} U_{ij}\left(r_{ij}\right) + \sum_i F_i(\bar{\rho}_\iota) \quad (4)$$

$$\bar{\rho}_\iota = \sum_{i\neq j} \rho_j(r_{ij}) \quad (5)$$

Where $U_{ij}(r_{ij})$ is the pair atomic interactions. ρ_j is the electron density contribution of atom j and $\bar{\rho}_\iota$ is the average total contribution from all atoms to the electron density at the position of atom i. $F(\bar{\rho}_\iota)$ represents the many-body behavior and approximates the energy required to insert the ionic cores into the electron density [23], [51], [53].

In our new proposed hybrid EABC potential, for the interactions between Cs-Cs and Pb-Pb, the Buckingham part of the potential shown in Equation 1 is replaced by the EAM potential shown in Equation 4 while the Coulomb potential is still imposed. The new Hybrid EABC potential parameters are summarized in Table 3-2.

Table 3-2: Hybrid EABC Potential Model Parameters of $CsPbI_3$ [44]

***C**oul-**B**uck Interactions*	$A\ (eV)$	$\rho\ (\dot{A})$	$C\ (eV\dot{A}^6)$	*Ion*	*Effective Charge*
Cs-Pb	3.3068x1011	0.10519	0.0	Cs Pb I	1.36 2.03 -1.13
Cs-I	4913.000	0.3814	480.06		
Pb-I	4488.05	0.321737	0.0		
I-I	988.42	0.482217	30.22285		
Coul-EAM	Buck	EAM	Coul		
Cs-Cs	0	[133]	$Cs^{+1.36}$		
Pb-Pb	0	[134]	$Pb^{+2.03}$		

Details of the Molecular Dynamics Simulations

All classical molecular dynamics calculations are carried out using LAMMPS [130]. The bulk materials of 1920 atoms were generated by duplicating the unit cell of orthorhombic $CsPbI_3$ by 6 x 4 x 4 in the x-axis, y-axis, and z-axis respectively by ATOMSK code [135] , and periodic boundary conditions were applied. Periodic boundary conditions, PBC, are used to represent the bulk material by satisfying relation 3.3 as shown in Figure 3-1.

$$\begin{cases} if\ r_{ix} \geq {}^{L_x}/_{2}, & Replace\ it\ by\ r_{ix} - L_x \\ if\ r_{ix} \leq -{}^{L_x}/_{2}, & Replace\ it\ by\ r_{ix} + L_x \end{cases} \quad 3.3$$

where r is the position of an atom and L is the simulation box edge.

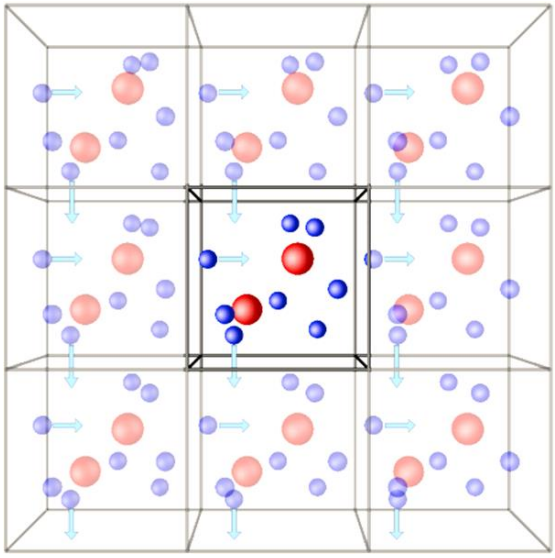

Figure 3-1: Representation of the periodic boundary conditions. This figure is inspired by [23].

The calculation of forces is highly demanding, and hence a cutoff radius should be defined where the potential gradually dies out. For both force fields, the cutoff radius was set to be 12 Å based on iterations to produce the most reliable structure at room temperature.

For every 100 timesteps, temperature, density, and simulation box edges were calculated. The system first equilibrates at room conditions, room temperature, and atmospheric pressure, with a time step of 0.5 femtoseconds (fs) for 30 ps to study the density and structural properties at room conditions. Temperature is then raised to study the phase transition. This is achieved by the Isobaric-Isothermal ensemble, NPT, which applies the Nose-Hoover thermostat and barostat [136]. In the case of Coul-Buck, the temperature is raised at a rate of 100K every 16 ps. However, in Hybrid EABC, a more considerable time is needed to ensure proper equilibration and temperature control; hence the temperature is raised at 100K every 48 ps. The visualization of the structure was carried by OVITO [137] , and the postprocessing was carried out in MATLAB.

Chapter 4

Results and Discussion

4.1 The Structural Properties of $CsPbI_3$ from DFT Calculations

Accurate prediction of the crystal system and the structural properties, including lattice parameters and bond lengths, are important in predicting perovskites' overall performance. Figure 4-1 shows $CsPbI_3$ in the ideal cubic perovskite structure where Cs^+ lies in the 12-fold coordination in the middle of a cube of eight corner-sharing of PbI_3 octahedra. The Cubic $CsPbI_3$ belongs to the space group of $Pm\bar{3}m$ and it is known as the black polymorph and is represented by α-$CsPbI_3$ [138].

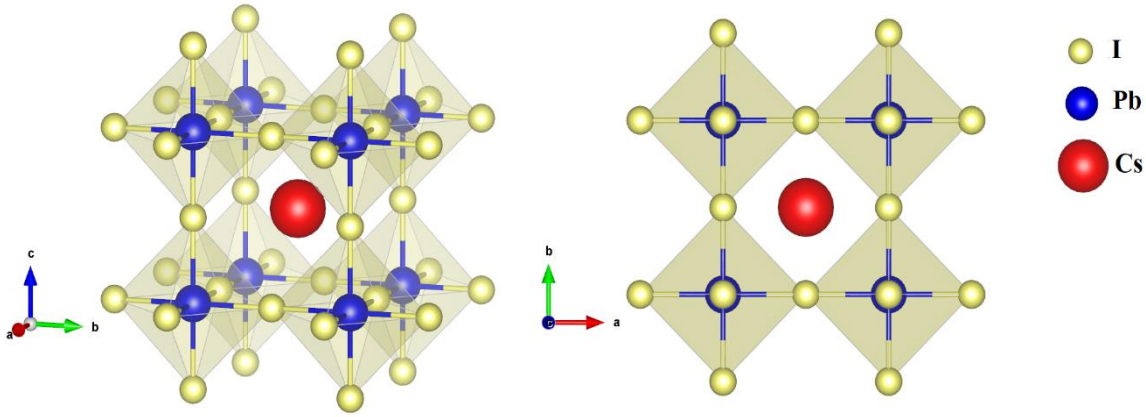

Figure 4-1: Cubic $CsPbI_3$ 3D structure with polyhedra (Left) and 2D projection on ab plane (Right) (Red: Cs, Blue: Pb, Yellow: I).

The α-$CsPbI_3$ was not stable at room temperature. Instead, the $CsPbI_3$, which was stable at room temperature, has an orthorhombic structure that belongs to the space group Pnam [113], [138]. This polymorph is known as the yellow non-perovskite δ-$CsPbI_3$ and it is considered as the most stable form in the ambient conditions [12], [113], [138], [139]. The δ-$CsPbI_3$ is shown in Figure

4-2. This phase's structural properties and its transformation into the cubic phase are modeled and discussed in the following sections.

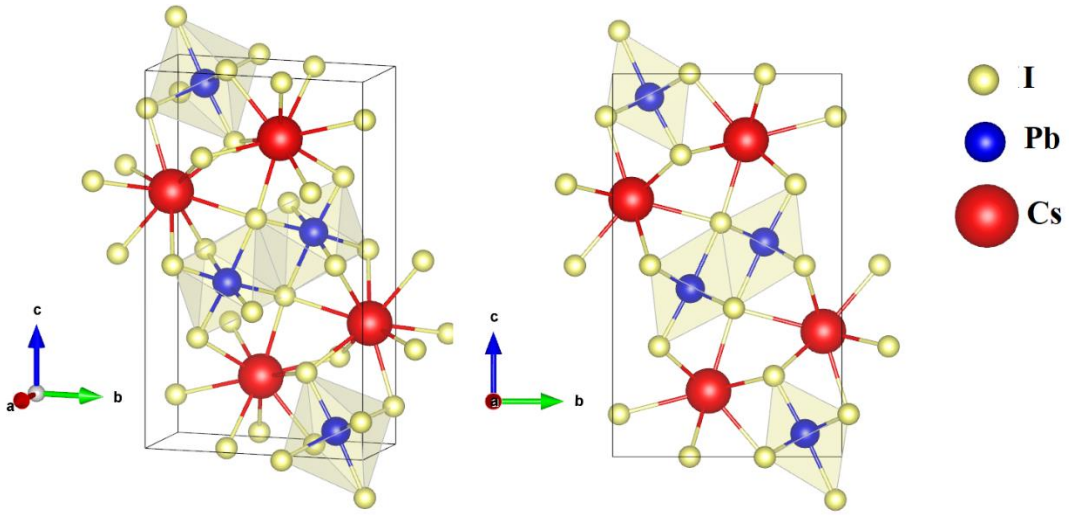

Figure 4-2: Orthorhombic Yellow $CsPbI_3$ 3D structure with polyhedra (Left) and 2D projection on bc plane (Right) (Red: Cs, Blue: Pb, Yellow: I).

It has been confirmed that the room-temperature black polymorph of $CsPbI_3$ is an orthorhombic perovskite with space group Pnam [138]. This polymorph is obtained by rapid cooling from the cubic phase and is known as the quench-cooled black phase(γ-$CsPbI_3$). The γ-$CsPbI_3$ is shown in Figure 4-3. It is worth noting that γ-$CsPbI_3$ decomposes into δ-$CsPbI_3$ upon exposure to moist air which as was mentioned earlier, is not a perovskite phase.

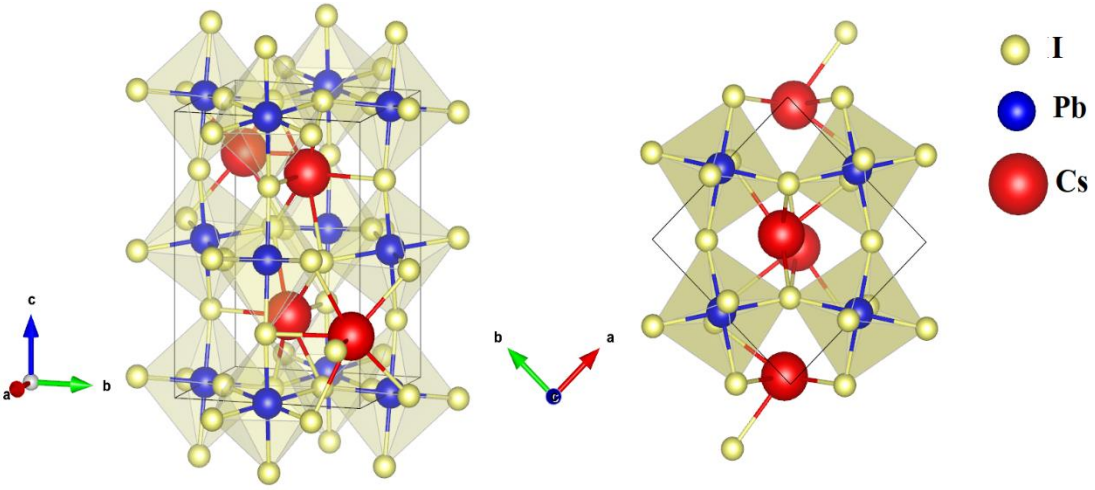

Figure 4-3: Orthorhombic Black $CsPbI_3$ 3D structure with polyhedra (Left) and 2D projection on ab plane (Right) (Red: Cs, Blue: Pb, Yellow: I).

The lattice parameters and volume of the optimized polymorphs of $CsPbI_3$ with both functionals: PBE and PBEsol, are reported in Table 4-1. For α-$CsPbI_3$, the PBE overestimates the experimental lattice parameter of 6.289 Å reported in [140] by ~1.65%, while the PBEsol underestimates the α-$CsPbI_3$ experimental lattice parameter by ~0.7%. For the γ-$CsPbI_3$, the experimental lattice parameters: a, b and c were found to be 8.856 Å, 8.576 Å, and 12.472 Å, respectively [138]. PBE overestimates the lattice parameters of γ-CsPbI3 with an average of ~2.15% with a maximum of 2.93% in predicting a while PBEsol underestimates the lattice parameters with an average of ~0.56%. For the δ-CsPbI3, the experimental lattice parameters: a, b and c were found to be 4.799 Å, 10.462 Å, and 17.765 Å, respectively [138]. The PBE overestimates the lattice

Table 4-1: Lattice Parameters and Volume of $CsPbI_3$ Polymorphs

Items	**α-$CsPbI_3$**	**γ-$CsPbI_3$**	**δ-$CsPbI_3$**
Colour	Black	Black	Yellow
Crystal structure	Cubic	Orthorhombic	Orthorhombic
Space group	$Pm\bar{3}m$	Pnam	Pnam
Z	1	4	4
No. of Atoms	5	20	20
	PBE		
Lattice parameters (Å)	a = b = c = 6.39286	a = 8.82731	a = 4.87871
		b = 8.98673	b = 10.81191
		c = 12.72858	c = 18.21317
Angles (°)	$\alpha = \beta = \gamma = 90$	$\alpha = \beta = \gamma = 90$	$\alpha = \beta = \gamma = 90$
Volume ($Å^3$)	261.2675	1009.741	960.712
	PBEsol		
Lattice parameters (Å)	a = b = c = 6.24556	a = 8.39309	a = 4.76046
		b = 8.93628	b = 10.41718
		c = 12.41385	c = 17.65860
Angles (°)	$\alpha = \beta = \gamma = 90$	$\alpha = \beta = \gamma = 90$	$\alpha = \beta = \gamma = 90$
Volume ($Å^3$)	243.6200	931.0760	875.6995

parameters of δ-$CsPbI_3$ with an average of ~2.5% with a maximum of 3.34% in predicting b. While PBEsol underestimates the lattice parameters with an average of ~0.6%. The PBEsol outperforms the PBE in predicting the structural parameters of $CsPbI_3$ polymorphs. This could be due to the fact that PBEsol usually works better in predicting the structural properties of close-packed structures.

4.2 The Structural Properties of $CsGeI_{3-x}Br_x$ from the DFT Calculations

In $CsGeI_3$, where Ge^+ replaces Pb^+, it offers a solution to the toxicity issue of lead. The $CsGeI_3$ deviates from the cubic structure and has a trigonal (rhombohedral) crystal structure with the space group of R3m. The trigonal $CsGeI_3$ is stable at ambient conditions [13]. Figure 4-4 shows $CsGeI_3$ with two axes representations. The first representation is the hexagonal with z =3 and 15 atoms. The second representation is the rhombohedral representation with z = 1 and 5 atoms. In the rhombohedral representation, the Cs^+ cation is at the corners of the rhombohedron, I^- anions are in the face-centered positions, and the Ge cation is at the body-centered position of the rhombohedron.

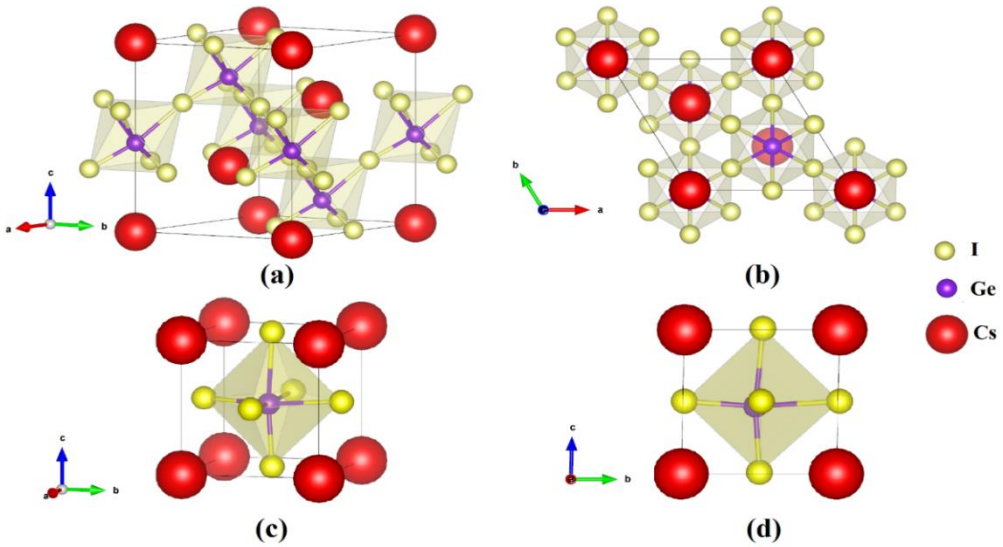

Figure 4-4: (a) $CsGeI_3$ 3D structure Z =3 with polyhedra (b) 2D projection of $CsGeI_3$ (Z =3) on ab plane (c) $CsGeI_3$ 3D structure Z =1 with polyhedra and (d) 2D projection of $CsGeI_3$ (Z =1) on bc plane (Red: Cs, Purple: Ge, Yellow: I).

$CsGeI_3$ has a narrow bandgap that is much smaller than the optimum bandgap required for photovoltaic applications. Therefore, we investigated the option of doping the structure with Br- to increase the bandgap. Our calculations showed that the $CsGeI_{3-x}Br_x$ compounds belong to the crystal rhombohedral structure with space group R3m. The optimized structures of the $CsGeI_{3-x}Br_x$ with x = 1, 2, and 3 are shown in Figure 4-5 with the 2D projection on both bc and ab planes.

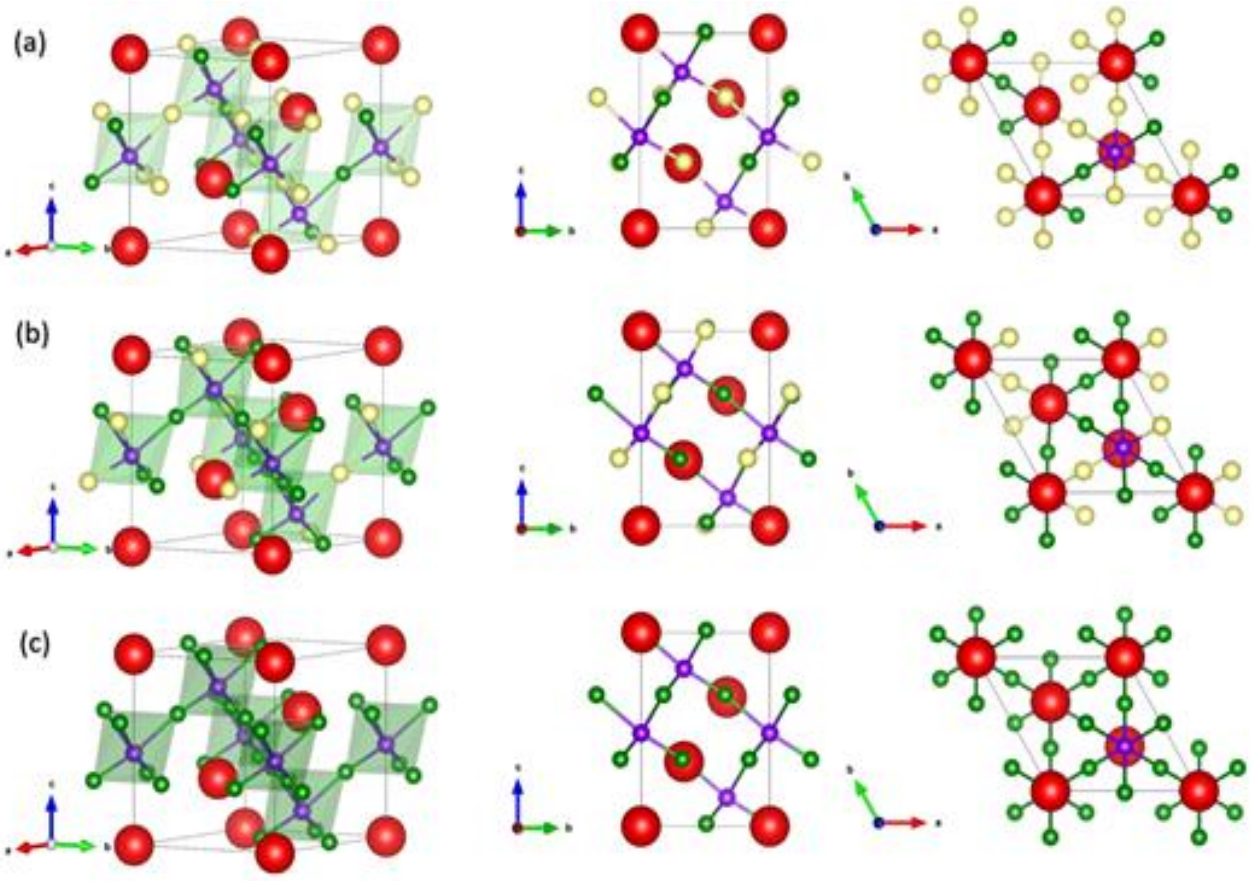

Figure 4-5: 3D structure with polyhedra (right), 2D projection on bc plane (left) and 2D projection on ab plane (middle) of (a) $CsGeI_2Br$, (b) $CsGeIBr_2$, and (c) $CsGeBr_3$. The bonds that are shown are only Ge-X bonds. (Red: Cs, Purple: Ge, Yellow: I, Green: Br)

The lattice parameters and volume of the optimized trigonal $CsGeI_{3-x}Br_x$ with both functionals: PBE and PBEsol, are reported in Table 4-2. The angles are slightly less than $90^{o,}$ which slightly deviates the structure from the cubic perovskite structure. For the $CsGeI_3$, the rhombohedral lattice parameter's experimental values are 5.98285 Å and 5.9830 Å as reported in [13] and [66], respectively. The PBE, as expected, overestimates the experimental lattice parameters with a ~1.6% increase, while the PBEsol underestimates the experimental lattice parameter with almost the same percentage. For the pure $CsGeBr_3$, the rhombohedral experimental lattice parameter was measured to be 5.6359 Å and 5.6375 Å as reported in [66] and [141], respectively. The lattice parameter obtained by the PBE is closer to the experimental value than the lattice parameter obtained by the PBEsol. The PBE overestimates the experimental lattice parameter of $CsGeBr_3$ by ~1.6%, while the PBEsol underestimates the experimental lattice parameter by ~2%. The PBEsol outperforms the PBE in calculating the lattice parameters a and b in $CsGeI_3$ and $CsGeBr_3$, while the PBE outperforms the PBEsol in calculating c in both compounds.

The PBE overestimates the volume of $CsGeI_3$ with ~4.8%, while the PBEsol underestimates the volume of $CsGeI_3$ with nearly the same percentage. On the other hand, the PBE slightly outperformed the PBEsol for the volume calculations in $CsGeBr_3$. Our computations showed that the iodine anions' replacement by the smaller bromine anions reduces the lattice parameter and the unit cell volume. Additionally, with the increase in the bromine content, the unit cell becomes closer to the cubic behavior as the deviation from the right angle of the ideal cubic structure becomes smaller, which might result in higher structural stability.

Table 4-2: Lattice Parameters and Volume of $CsGeI_{3-x}Br_x$ mixed halides.

Items	**$CsGeI_3$**	**$CsGeI_2Br$**	**$CsGeIBr_2$**	**$CsGeBr_3$**
x	0	1	2	3
Crystal structure	Trigonal	Trigonal	Trigonal	Trigonal
Space group	R3m	R3m	R3m	R3m
	PBE			
Edge Length (Å)				
Rhombohedral Axes	a = 6.07765	a = 6.00180	a = 5.89114	a = 5.72812
Angle (°)	$\alpha = 88.6605$	$\alpha = 88.6241$	$\alpha = 88.8227$	$\alpha = 88.8289$
Hexagonal Axes	a = b = 8.494	a = b = 8.385	a = b = 8.245	a = b = 8.0176
	c = 10.770	c = 10.642	c = 10.411	c = 10.122
Angle (°)	$\alpha = \beta = 90, \gamma = 120$	$\alpha = \beta = 90, \gamma = 120$	$\alpha = \beta = 90, \gamma = 120$	$\alpha = \beta = 90, \gamma = 120$
Volume ($Å^3$)	672.943	648.031	612.983	563.494
	PBEsol			
Edge Length (Å)				
Rhombohedral Axes	a = 5.88370	a = 5.80955	a = 5.70651	a = 5.52277
Angle (°)	$\alpha = 89.1833$	$\alpha = 89.1823$	$\alpha = 89.2670$	$\alpha = 89.2675$
Hexagonal Axes	a = b = 8.261	a = b = 8.157	a = b = 8.0184	a = b = 7.760
	c = 10.335	c = 10.205	c = 10.01	c = 9.687
Angle (°)	$\alpha = \beta = 90, \gamma = 120$	$\alpha = \beta = 90, \gamma = 120$	$\alpha = \beta = 90, \gamma = 120$	$\alpha = \beta = 90, \gamma = 120$
Volume ($Å^3$)	610.860	588.054	557.350	505.226

4.3 The B-X bond lengths for $CsPbI_3$ and $CsGeI_{3-x}Br_x$ from the DFT Calculations

The B (Pb or Ge) cation and X (I, Br, $I_{3-x}Br_x$) halide bond length is another important halide perovskite's structural property. The bond length is a direct indication of the bond strength which significantly affects the structure stability and indirectly affects the electronic and optical properties. The calculated bond lengths of Pb-I for $CsPbI_3$ polymorphs and Ge-X for $CsGeI_{3-x}Br_x$ are reported in Table 4-3. The octahedra of α-$CsPbI_3$ are highly ordered and symmetric with equal Pb-I lengths. The experimental value for the Pb-I bond length in α-$CsPbI_3$ is 3.1447 [140]. As shown in Table 4-3, PBE overestimates the Pb-I bond length experimental value by ~1.64%, while PBE sol underestimates it by ~0.7%.

In γ-$CsPbI_3$, we observed that the Pb-I bonds are divided into three sets of pairs of equal bonds. Our calculated values with both PBE and PBEsol agreed well with the fact that Pb-I bonds are expected to lie between 3.15 to 3.22 Å [138]. However, for δ-$CsPbI_3$, Pb-I's bond lengths were divided into four groups: one short apical bond, two equal short equatorial bonds, two equal long equatorial bonds, and one long apical bond. This behavior agrees with the experimental values reported in [140]. These bonds' experimental values are 3.0513, 3.2259, 3.2775, and 3.4076, respectively [140]. PBEsol outperforms PBE in predicting the equatorial bonds and the short apical one. However, the PBE estimates the long apical bond better.

On the other hand, for all Ge-based compounds, the octahedra are distorted. The Ge-X bonds in $CsGeI_3$ and $CsGeBr_3$ are divided into two types of bonds. One is a short bond with strong covalent interaction, and the other is a long bond with a weaker interaction. This difference in the bond lengths could be explained by the Ge offset from the cell center position observed in Figure 4-4 (c) and (d). Our results showed that the Ge offset decreased with the increase of Br content. The experimentally reported values of Ge-I bonds in $CsGeI_3$ are 2.7723 Å and 3.4463 Å [13]. The experimentally reported values of Ge-Br bonds in $CsGeBr_3$ are 2.534 Å and 3.116 Å [141]. Both

PBE and PBEsol results for Ge-X agreed well with these experimental values. However, PBE surpasses PBEsol in these calculations.

Generally, the Ge-Br bond is shorter than the Ge-I bond. Our calculations showed that as the Br content increased in $CsGeI_{3-x}Br_x$, the average Ge-X bond length decreased. The octahedra in the mixed halide structures were highly distorted with six different bond lengths. Also, the Ge-X bonds can be divided into two types of bonds, short ones, and long ones, as shown in Table 4-3.

Table 4-3: Calculated B-X Bond lengths. (Numbers in brackets indicate the repetition of the corresponding value in a single octahedron)

B-X bond lengths (Å)						
α-$CsPbI_3$	**γ-$CsPbI_3$**	**δ-$CsPbI_3$**	**$CsGeI_3$**	**$CsGeI_2Br$**	**$CsGeIBr_2$**	**$CsGeBr_3$**
PBE						
(6) 3.19643	(2) 3.22871 (2) 3.23584 (2) 3.24269	(1) 3.11430 (2) 3.28344 (2) 3.32028 (1) 3.45210	(3) 2.79997	(1) 2.58724 (1) 2.77227 (1) 2.83574	(1) 2.55410 (1) 2.62391 (1) 2.78638	(3) 2.58550
			(3) 3.30836	(1) 3.22879 (1) 3.31145 (1) 3.36095	(1) 3.21439 (1) 3.32457 (1) 3.25537	(3) 3.16041
PBEsol						
(6) 3.12278	(2) 3.16322 (2) 3.17449 (2) 3.18168	(1) 3.07998 (2) 3.21170 (2) 3.25584 (1) 3.33550	(3) 2.78934	2.56906 2.73593 2.84221	(1) 2.52579 (1) 2.65818 (1) 2.74550	(3) 2.60213
			(3) 3.11533	3.00939 3.17055 3.18727	(1) 3.00993 (1) 3.08783 (1) 3.14990	(3) 2.92817

4.4 Structural Properties of $CsPbI_3$ at Room Temperature Using CMD

The Orthorhombic Yellow $CsPbI_3$, δ-$CsPbI_3$, in Figure 4-6, is duplicated and equilibrated at ambient conditions using Classical Molecular Dynamics, CMD. The supercells of $CsPbI_3$ with 1920 ions at the ambient condition from the CMD calculations using the Buckingham-Coulomb and the new proposed Hybrid EABC forces fields are shown in Figure 4-6. The structure resulting from the Hybrid EABC potential (Figure 4-6.b) is more ordered than the one resulted from the Buckingham-Coulomb potential (Figure 4-6.a). The radial distribution functions of bulk $CsPbI_3$ at 300K using the Buckingham-Coulomb potential and Hybrid EABC potential were obtained using 100 bins and shown in Figure 4-7 and Figure 4-8, respectively.

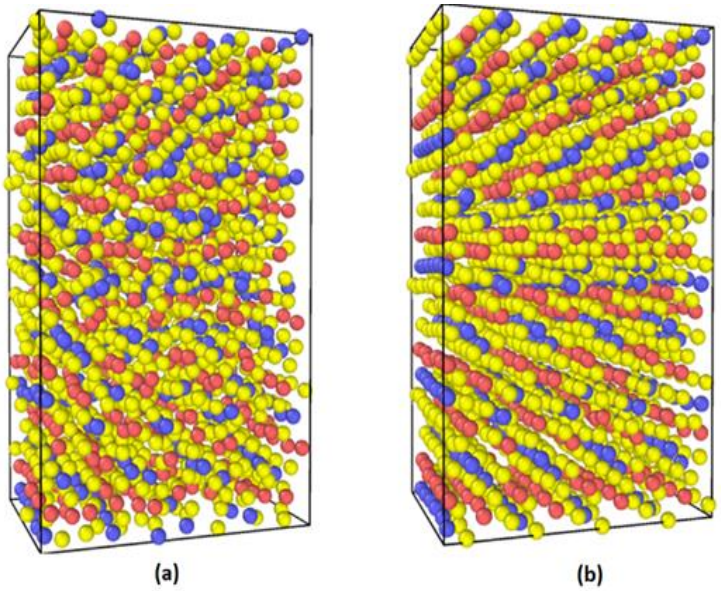

Figure 4-6: The orthorhombic structures from CMD calculations at ambient conditions (Yellow: I, Red: Cs and Blue: Pb) (a) Orthorhombic structure after equilibration using Buckingham– Coulomb potential (b) Orthorhombic structure after equilibration using Hybrid EABC potential [44]

One significant difference between the outcomes of using the two potentials occurs in the Pb-I interaction, where the Buckingham-Coulomb peak is shifted to the right with ~0.15 Å compared to the Hybrid EABC peak. Moreover, both Cs-Pb and Pb-I peaks from the Hybrid EABC potential agree with the radial distribution functions resulting from the DFT calculations shown in Figure 4-9, which implies that EAM potential inclusion in the Hybrid EABC helps to maintain the integrity of the initial orthorhombic structure. Moreover, the peaks resulting from using the hybrid potential are closer to the peaks of the radial distributions functions, which were obtained experimentally [142] and are shown by the dotted red lines in Figure 4-7 and Figure 4-8.

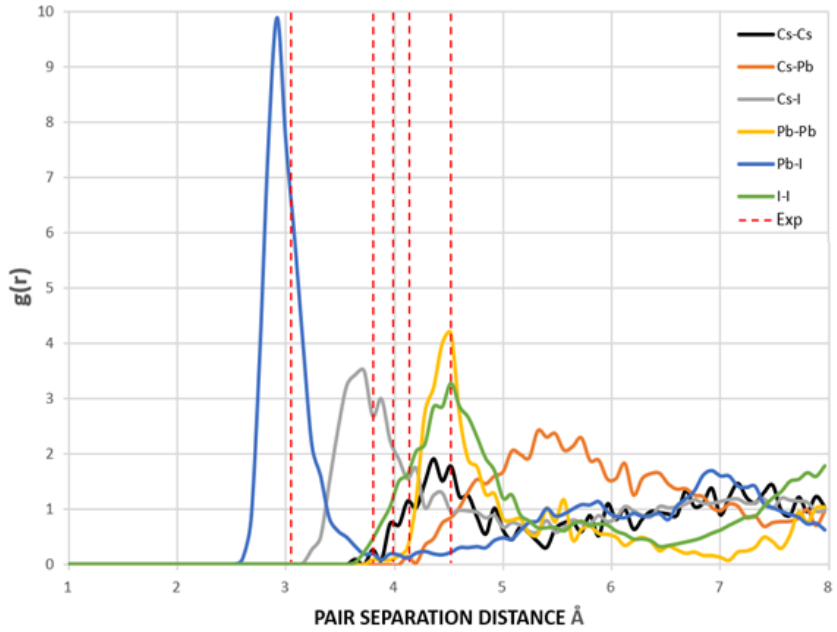

Figure 4-7: The Radial Distribution Function of the Equilibrated Structure with Buckingham-Coulombs at 300 K and g(r) with 100 bins (Yellow: I, Red: Cs and Blue: Pb) [44]. The experimental values are obtained from [142]

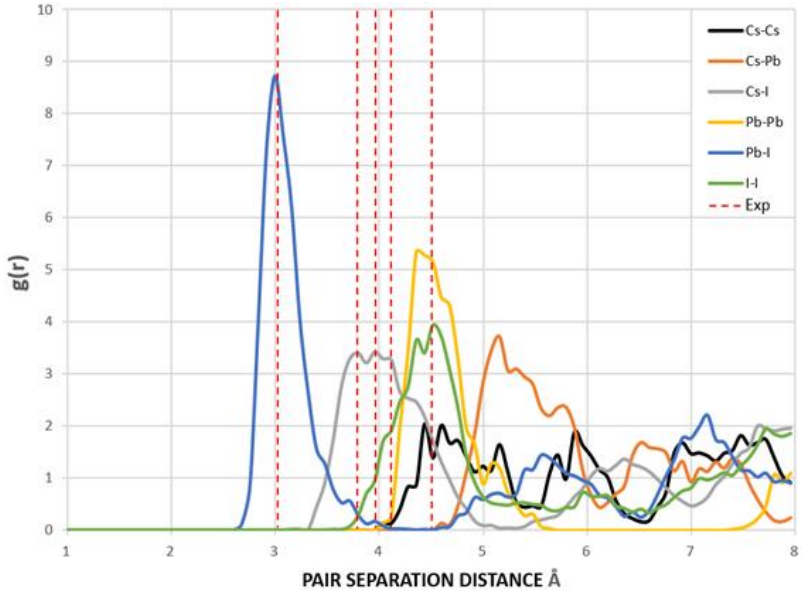

Figure 4-8: The Radial Distribution Function of the Equilibrated Structure with Hybrid EABC at 300 K and g(r) with 100 bins (Yellow: I, Red: Cs, and Blue: Pb) [44]. The experimental values are obtained from [142]

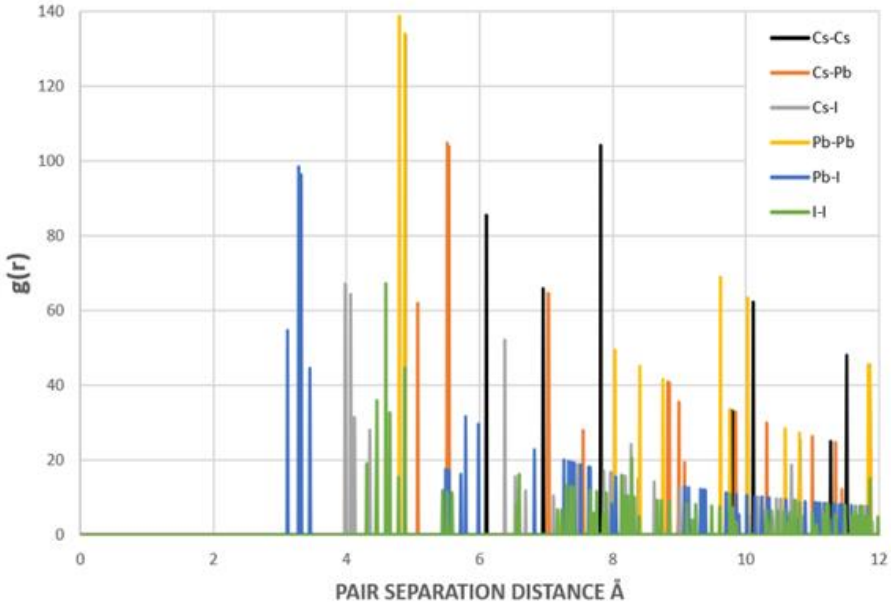

Figure 4-9: Radial Distribution Function of the structure that resulted from DFT and inputted to MD. This RDF was generated by 1000 bins [44]

The interatomic separation distances between the different ions using the Buckingham Coulomb and Hybrid EABC potential functions were obtained from RDF with 1000 bins for higher accuracy and are reported in Table 4-4. The largest deviation occurs at the Cs-Pb interaction when comparing the outcomes of the two force fields. The Buckingham-Coulomb Cs-Pb peak is shifted ~0.4 Å to the left of the Hybrid EABC peak. Simultaneously, the slightest deviations occur at Cs-Cs and I-I peaks with a departure of ~0.01 Å.

Table 4-4: Rhombohedral $CsGeI_3$ lattice parameters and volume [44]

Interaction	**Interatomic Distance(Å)**	
	Coul-Buck	**Hybrid EABC**
Cs – Cs	4.4820	4.4700
Cs – Pb	5.3820	4.9860
Cs – I	3.6900	3.7500
Pb – Pb	4.4820	4.5180
Pb – I	2.9100	3.0540
I – I	4.5180	4.5060

The newly proposed Hybrid EABC results in Pb-I bond lengths of ~3.05 Å, which agrees with experimental findings reported by Straus et al. [142] with an error of less than 1%. Also, it proves that the change in lattice parameters with temperature must originate from tilting in the octahedra of Pb-I. The accuracy of modeling Pb-I interaction is crucial in modeling lead iodide perovskites as the electronic and optical properties are much dependent on this bond [143].

It is worth noting that when the structure was equilibrated with the Hybrid-EABC force field but with omitting the Cs-Cs and Pb-Pb coulomb interactions, the orthorhombic form clustered into CsI and PbI_2 as shown in Figure 4-10. This clustering behavior demonstrates the experimental method of mixing CsI and PbI_2 [113] to produce $CsPbI_3$ but in reverse. Also, this implies the significance of coulombic interactions between Cs-Cs and Pb-Pb in stabilizing the structure.

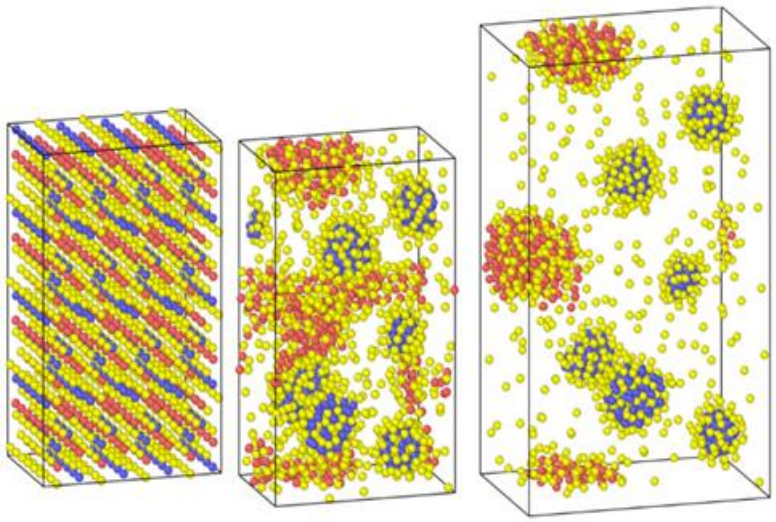

Figure 4-10: Clustering of $CsPbI_3$ as CsI and PbI_2 when the coulombic interactions are neglected between Cesium ions and between lead atoms [44]

The scatter plots of the X-Positions vs. Z-Positions of $CsPbI_3$ ions within the supercell at 0K, 300K, and 600K are shown in Figure 4-11. An apparent rattling behavior appeared in the scatter plot of the X-Positions vs. Z-Positions of at 300 K compared to 0K. This behavior can be attributed to the distortion of Cs atoms and Pb-I octahedra. Cs ions' highly distorted and irregular behavior can also be observed in our Cs-Cs interaction in the RDF results shown in Figure 4-7 and Figure 4-8. The Cs behavior agrees with the findings in [142] that Cs cations become distorted, occupy two positions, and rattle within the structure, causing the instability of $CsPbI_3$ at ambient conditions. At 600 K, the increase in volume observed from the increase in the scattered positions along the X-axis indicates the transition into a cubic crystal structure. It would be discussed in more detail in the phase transformation section.

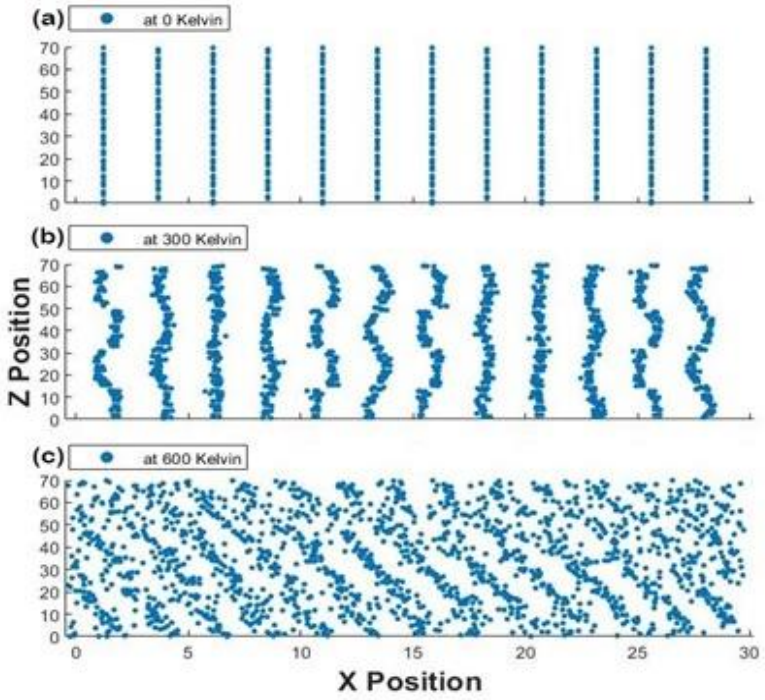

Figure 4-11: Scatter Plot of X Positions Vs Z Positions for the 1920 atoms at (a) 0 K, (b) 300 K, and (c) 600 K at one time for the Hybrid EABC Model [44]

The density of the orthorhombic structure, resulting from our DFT calculations, was 4.983 g/cm^3. After the equilibration using the Buckingham-Coulomb force field at 300 K, the structure density decreased to approximately 4.8 g/cm^3. On the other hand, when the full Hybrid EABC potential was used with 0.5 fs timestep, the density was 5.2558 g/cm^3. This value is only 2.5 % and 1.9% lower than the experimental density values of orthorhombic δ-$CsPbI_3$ reported in [113] and [140], respectively.

4.5 Phase Transition from Orthorhombic to Cubic $CsPbI_3$ from CMD Calculations

The change of density with temperature resulting from using the Buckingham- Coulomb (BC) potential is illustrated in Figure 4-12. The density slowly decreases with temperature until a significant change in slope occurs at the vicinity of 800 K. This change in the slope could be attributed to the melting of $CsPbI_3$ indicated by Sharma et al. [144]. However, this potential could not detect the transition from orthorhombic to cubic crystal structures obtained by Wang et al. [113].

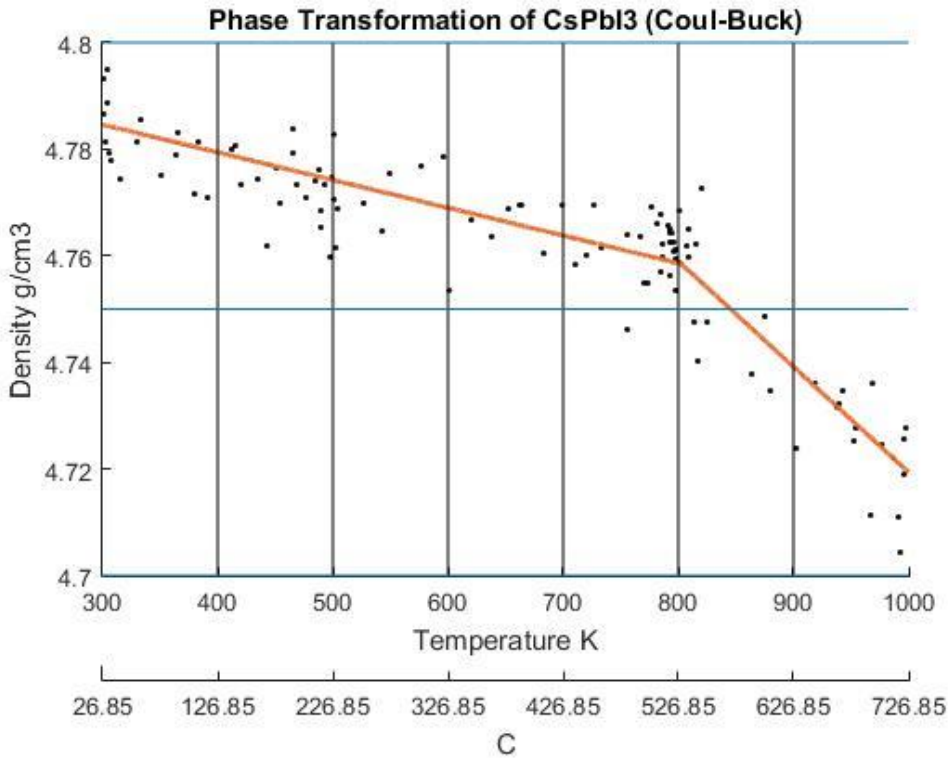

Figure 4-12: The density of $CsPbI_3$ as a function of temperature calculated by Buckingham-Coulombs. The scatter points represent measured points from the CMD model, and the orange curve is obtained by regression fitting [44]

Our new proposed Hybrid-EBC potential successfully reproduced the phase transition of $CsPbI_3$. The change of density with temperature calculated by the new Hybrid-EBC is shown in Figure 4-13. The density vs. temperature curve exhibits an abrupt change of density at different temperatures, indicating phase transformation. At 300 K, $CsPbI_3$ is stable as an orthorhombic structure with a density equal to 5.2558 g/cm^3, which is 2.5% less than the one reported experimentally by Wang et al. [113]. Then, the density decreases slowly as the temperature increases to ~560 K then an abrupt decrease in density starts at ~610 K, and it continues to fall till it reaches 4.81 g/cm^3 at 630 K. This could be attributed to the phase transformation from the orthorhombic to cubic structure, i.e., α-$CsPbI_3$. This agrees within 1.5 % with the experimental result by Trots et al. [140], which proved that CsPbI3 undergoes orthorhombic-to-cubic phase transition through two stages. The first starts at 563 K, where orthorhombic and cubic structures coexist, and the other is at 602 K, where the only cubic structure is present. During this phase transition, an increase in volume by 7.5% occurs, which is comparable to the experimental value of 6.9% reported in [140].

At 630 K, the density drops from 5.1 to 4.81 g/cm3. Simultaneously, the system's Nose-Hoover thermostat tries to maintain the system temperature at 600 K. This decrease in density and the increase in volume were also observed in the scatter plot of the X-Positions vs. Z-Positions at 600 K shown previously in Figure 4-11. Therefore, the system would eventually equilibrate at a density of 4.81g/cm3 at 600 K. The resulting structure is stable from ~593 K. The average temperature of the system from the beginning of the transformation till the end of the equilibration at the new phase is 594.6 K. These findings also perfectly match the experimental densities and the temperature reported by Wang et al. [113] and Trot et al. [140]. The experimental densities are indicated by the dashed lines in Figure 4-13. Further heating of the system results in a second change of slope at ~750 K, which might be attributed to melting, as reported by Sharma et al. [144].

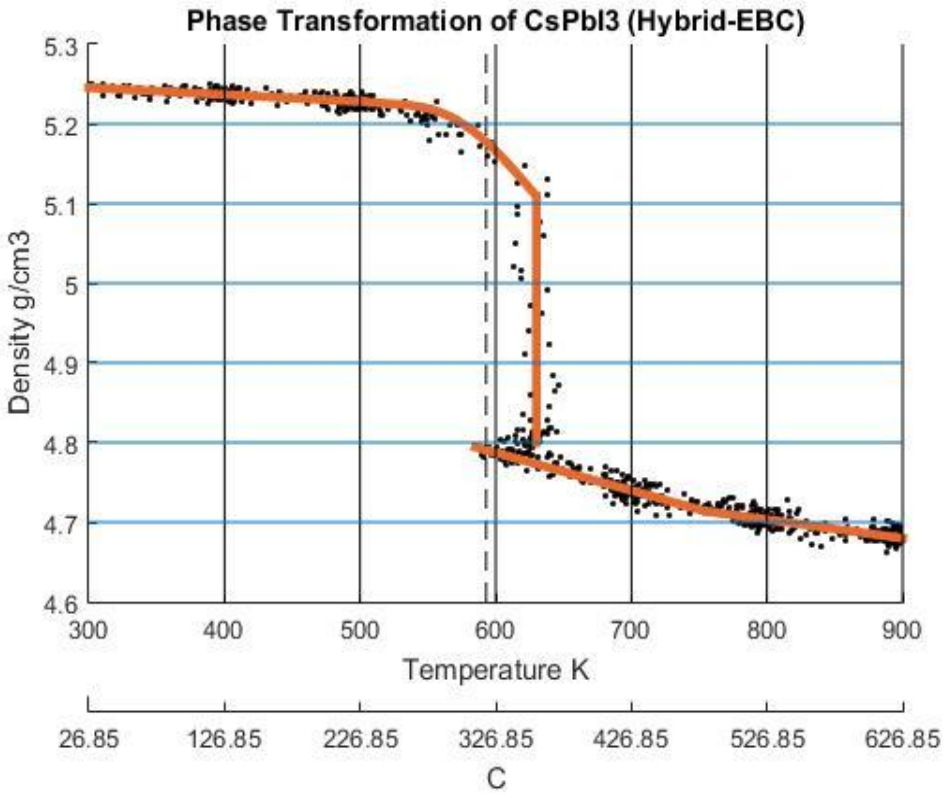

Figure 4-13: The density of $CsPbI_3$ as a function of temperature calculated by Hybrid EABC. The scatter points represent measured points from the CMD model, and the orange curve is obtained by regression fitting [44]. The red dashed lines represent iso-temperature lines obtained from experimental values in [137] , [112] , [141]

4.6 Electronic Properties of $CsPbI_3$ from the DFT Calculations

The two most important properties of materials for photovoltaic applications are the band structure and projected density of states (PDOS). The band structure reveals the energy bandgap and its type, either direct or indirect. The PDOS shows the atomic and orbital contribution to the electronic bandgap, giving insight into the bandgap engineering and optical properties. The band structure and the atomic PDOS of cubic $CsPbI_3$ are shown in Figure 4-14. The DFT simulates the band structure with reasonable accuracy but underestimates the band gaps [22], [145]. Our calculations showed that the α-$CsPbI_3$ has a direct bandgap of 1.4070 eV at point R (0.5,0.5,0.5) in the reciprocal space. The experimental bandgap of α-$CsPbI_3$ was reported to be ~1.73 eV [11]. Our result was closer to the experimental value as compared to the previous calculations of 1.11 eV by LDA [61] and 1.3 by FP–LAPW method within the generalized gradient approximation (GGA) [146]. It is clear from the right part of Figure 4-14 that Cs does not contribute to the band edge states while the iodine dominates the valence bands, and lead and iodine contribute to the conduction bands.

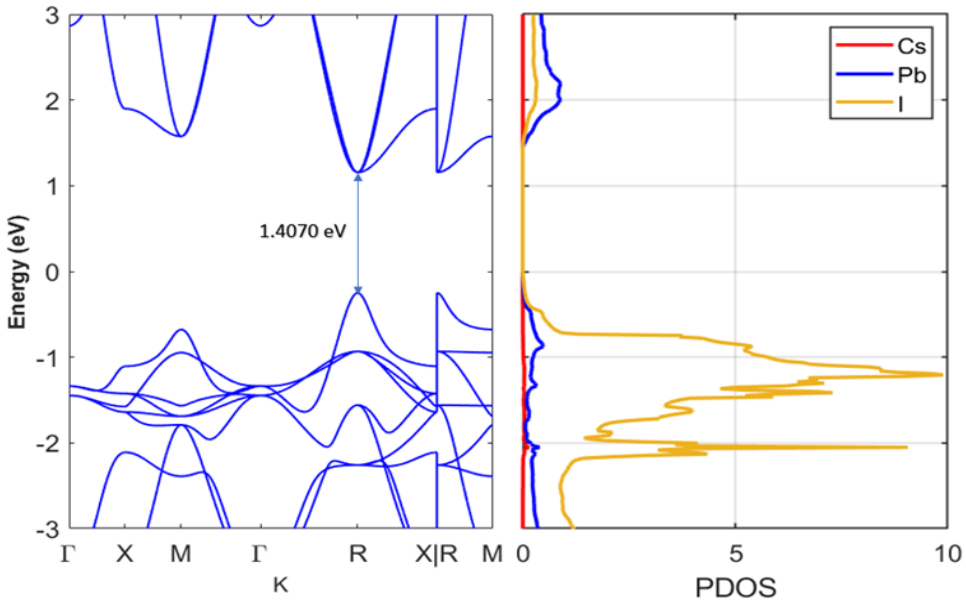

Figure 4-14: The Band Structure (left) and The Atom Projected Density of states (Right) of cubic $CsPbI_3$

Although the bandgap of α-$CsPbI_3$ is considered to have relatively an optimum bandgap, the material transforms into a yellow non-perovskite phase δ-$CsPbI_3$ at temperatures below 315 °C. Figure 4-15 shows the band structure and the density of states of δ-$CsPbI_3$. The conduction band minimum (CBM) occurs at (0.0, 0.469697, 0.0) while the valence band maximum (VBM) occurs at (0.181818, 0.0, 0.0) in the reciprocal space. Therefore, the bandgap is indirect and of 2.4969 eV, which deems this material very wide bandgap material. On the other hand, the quenched γ-$CsPbI_3$ has a direct bandgap of 1.7520 eV at the Gamma point (0.0,0.0,0.0), as shown in Figure 4-16. This bandgap value greatly agrees with the experimental value of 1.72 eV reported in [11] [147]. Although the bandgap of γ-$CsPbI_3$ is as interesting as the bandgap of α-$CsPbI_3$, the structure transforms to the insulating δ-$CsPbI_3$ upon exposure to moist air [138]. It is clear from the DOS plots in Figure 4-15 and Figure 4-16 that Cs does not contribute to the band edge states, iodine dominates the valence bands, and both Pb and I states contribute to the conduction bands.

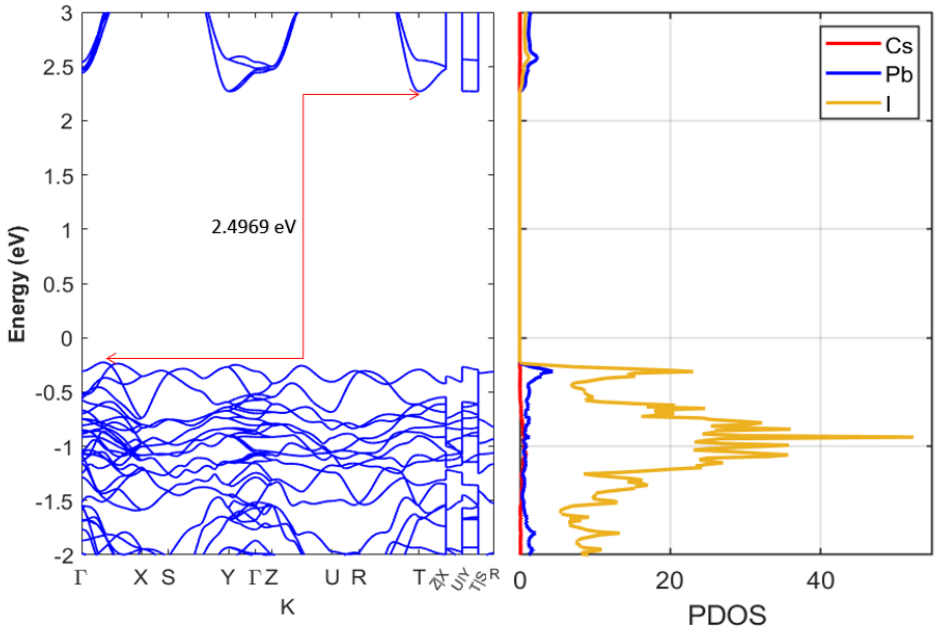

Figure 4-15: The Band Structure (left) and The Atom Projected Density of states (Right) of orthorhombic δ-$CsPbI_3$

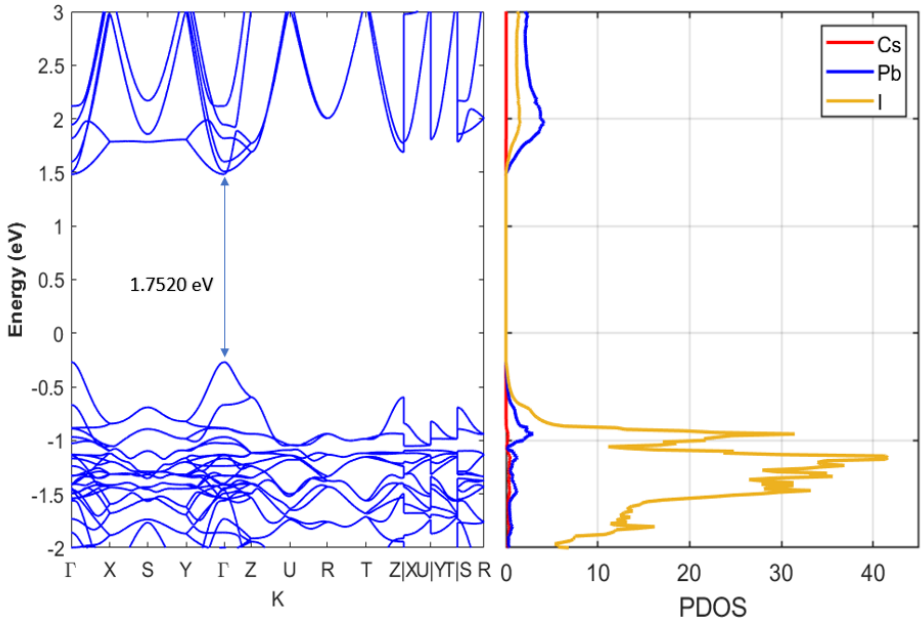

Figure 4-16: The Band Structure (left) and The Atom Projected Density of states (Right) of black orthorhombic $CsPbI_3$

4.7 The Electronic Properties of $CsGeI_{3-x}Br_x$ from the DFT Calculations

Replacing the lead cation in $CsPbI_3$ with germanium leads to $CsGeI_3$, a stable compound of R3m symmetry at ambient conditions. Figure 4-17 illustrates the band structure and atomic density of states of $CsGeI_3$. $CsGeI_3$ has its valence band maximum (VBM) and conduction band minimum (CBM) at Z (0,0,0.5) high symmetry point in the first Brillouin zone. Therefore, our calculations showed that $CsGeI_3$ is a direct bandgap material with a bandgap of 0.9639 eV. Even Though this calculated value underestimates the experimental value of 1.6 eV reported in [13] and 1.53 eV reported in [66] for $CsGeI_3$ bandgap, it is an improvement over the calculated value of 0.66 eV using LDA reported by [148]. The bandgaps of $CsGeI_3$ in the cubic phase were calculated using PBE to be 0.585 [149]. The difference in the bandgap values of the trigonal and cubic phase indicates a potential decrease in the bandgap upon the transformations from the trigonal to the cubic structure. However, a complete material decomposition was observed in $CsGeI_3$ before

transformation into cubic structure upon heating. Hence, a cubic system could not be obtained at a higher temperature [150]. As with $CsPbI_3$, Cs does not contribute to the edge states of the bandgap in $CsGeI_3$.

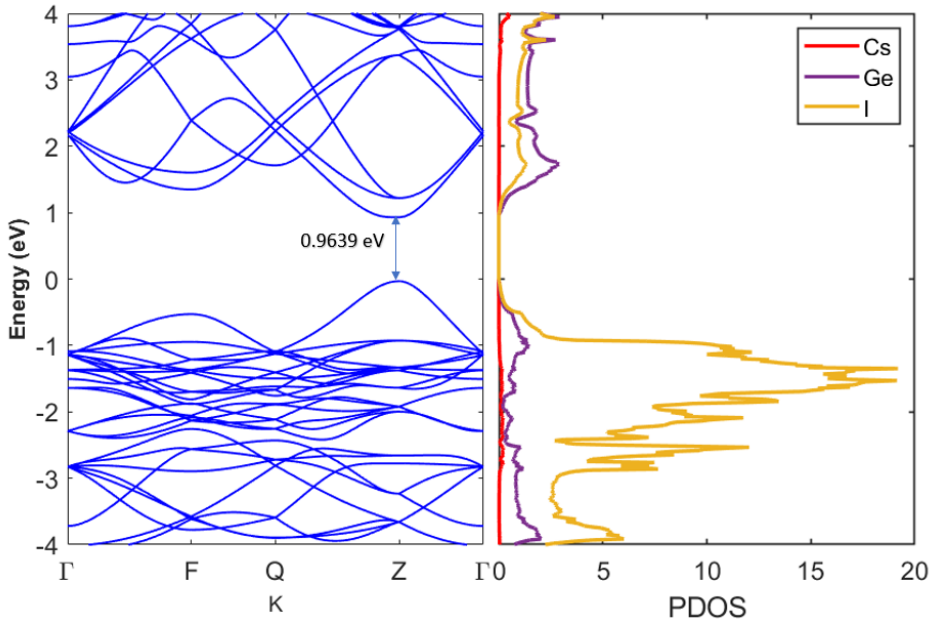

Figure 4-17: The Band Structure (left) and The Atom Projected Density of states (Right) of $CsGeI_3$

It would be of great technological importance for photovoltaic development, particularly in tandem solar cells, if we could tune the bandgap of halide perovskite. Driven by this notion, we investigated the electronic properties of $CsGeI_3$ doped with Br. Figure 4-18 and Figure 4-19 show the band structures and atomic density of states of the $CsGeI_2Br$ and $CsGeIBr_2$. Our calculations showed that both materials are direct bandgaps with a bandgap of 1.1085 and 1.2242 eV, respectively.

When Iodine is completely replaced with Br, the $CsGeBr_3$ is obtained. The band structure and atomic density of states of $CsGeBr_3$ are shown in Figure 4-20 with a direct bandgap of 1.307 eV. This calculated value underestimated the experimental values 2.38 eV reported in [141] and 2.32 eV reported in [66] for $CsGeBr_3$ $CsGeI_3$ bandgap. Yet, it is an improved estimate over the calculated value of 1.26eV using LDA reported by [148].

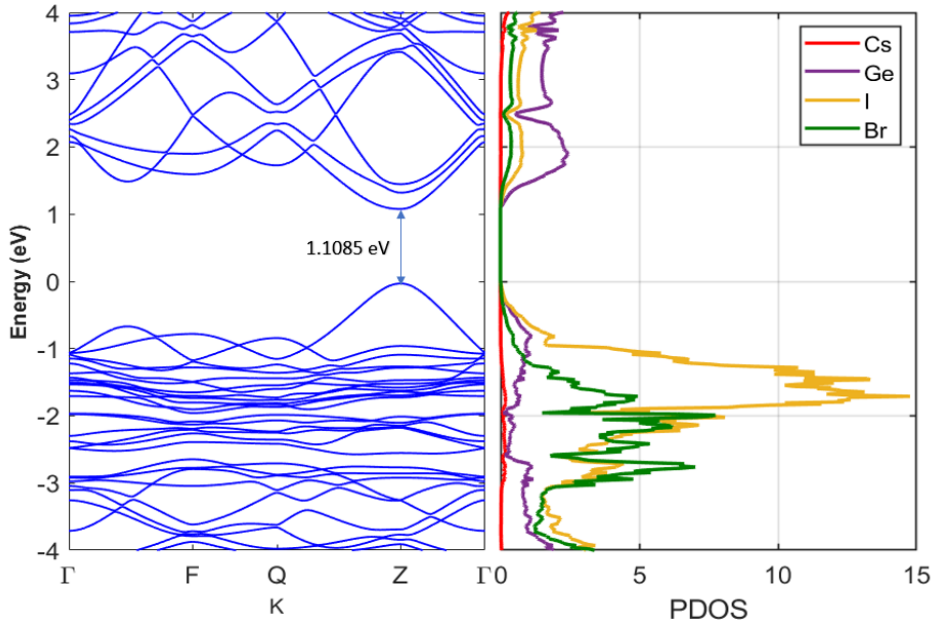

Figure 4-18: The Band Structure (left) and The Atom Projected Density of states (Right) of $CsGeI_2Br$

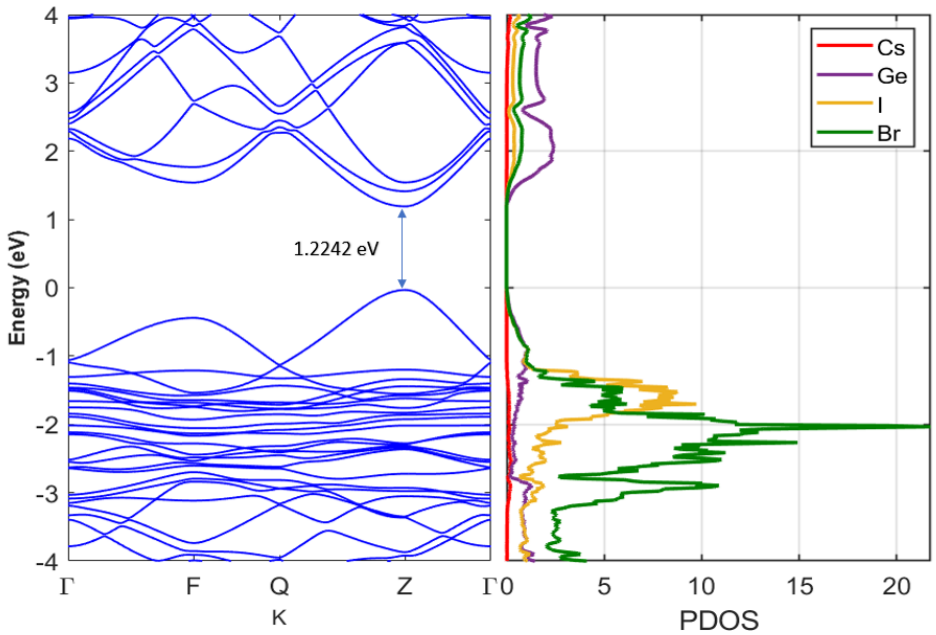

Figure 4-19: The Band Structure (left) and The Atom Projected Density of states (Right) of $CsGeIBr_2$

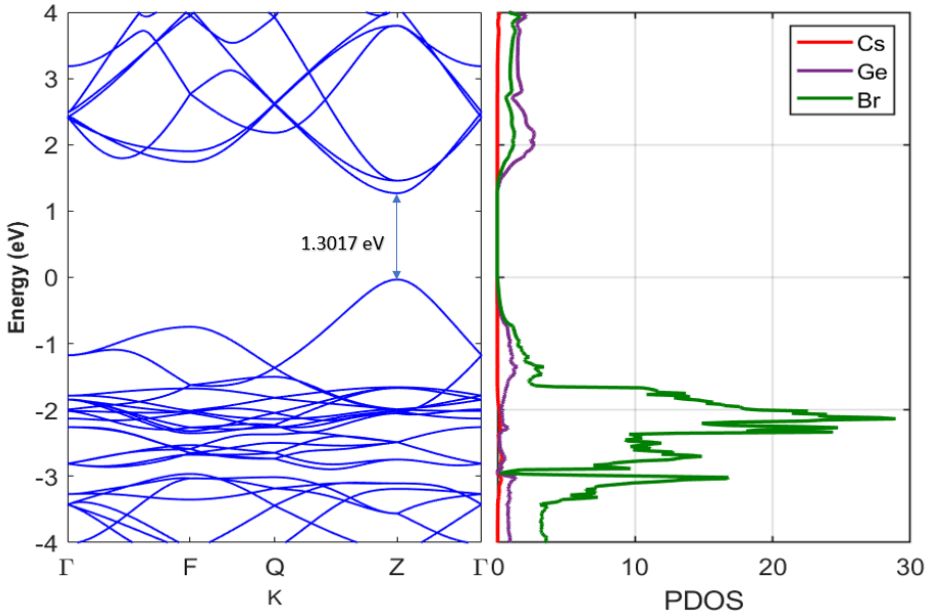

Figure 4-20: The Band Structure (left) and The Atom Projected Density of states (Right) of $CsGeBr_3$

The calculated bandgap of $CsGeI_xBr_{3-x}$ increased with increasing the Br^- content. The increase in the Br content resulted in a monotonic decrease in CBM eigenvalues' values, accompanied by a higher decrease in VBM eigenvalues' values. In fact, the increase in the values of the bandgap of $CsGeI_{3-x}Br_x$ going from x = 0 to x =3 manifested itself as a logarithmic increase. From the atomic density of states plots, Cs does not contribute to the edge states of the bandgap in all the materials of $CsGeI_xBr_{3-x}$, and the number of available states increases with the Br^- content.

4.8 The Orbital Projected DOS of $CsGeI_{3-x}Br_x$ and $CsPbI_3$ from the DFT Calculations

For a deeper understanding of the band edge states, we investigated the orbital density of states of all the previously discussed materials. Figure 4-21 shows the orbital projected density of states of the $CsPbI_3$, and Figure 4-22 shows the orbital projected density of $CsGeI_{3-x}Br_x$ from x = 0 to x = 3. It can be seen that Cs does not contribute to the band edge states. Additionally, no obvious DOS overlap is observed between Cs and I, indicating weak interactions between both ions.

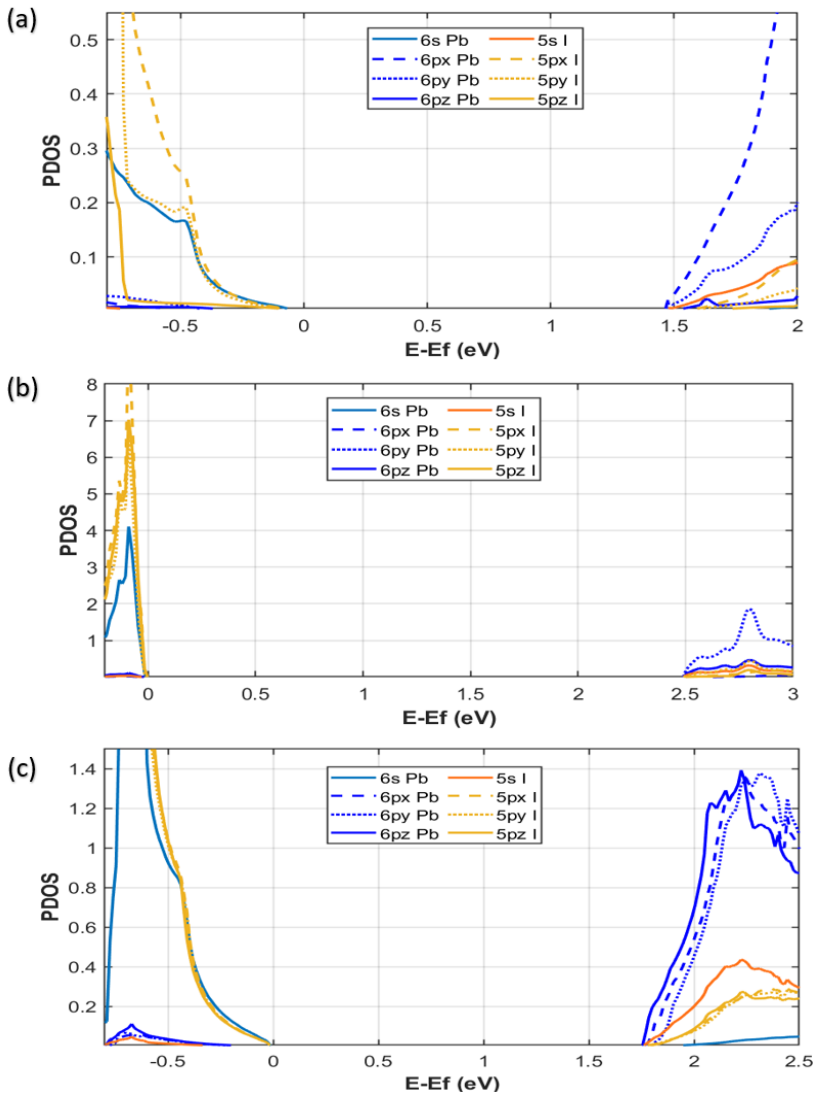

Figure 4-21: Orbital-projected density of states of (a) α-$CsPbI_3$ in the range from -0.5 eV to 2 eV, (b) δ-$CsPbI_3$ in the range from -0.3 eV to 3 eV, and (c) γ-$CsPbI_3$ in the range from -0.8 eV to 2.5 eV

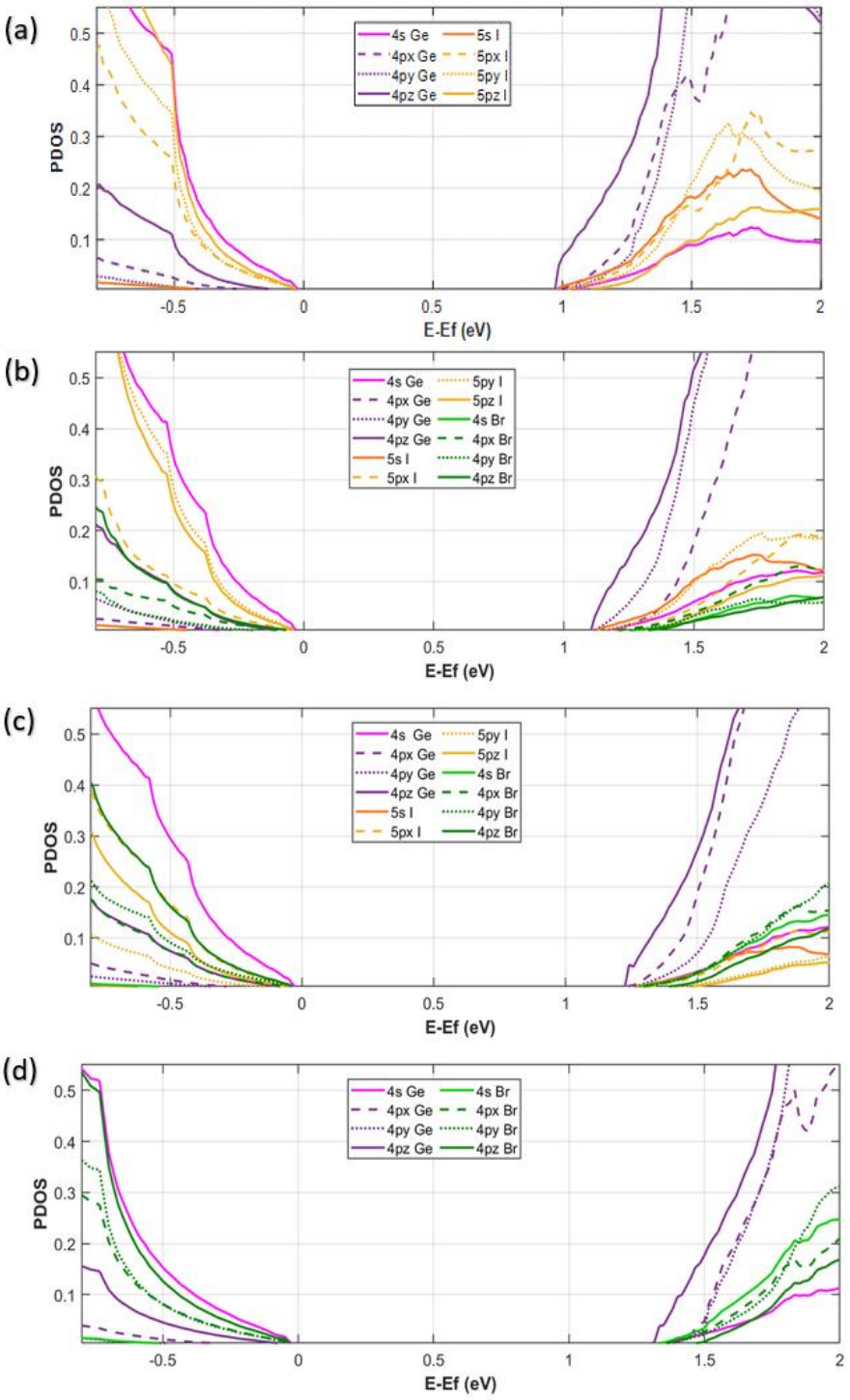

Figure 4-22: Orbital-projected density of states of trigonal (a) $CsGeI_3$, (b) $CsGeI_2Br$, (c) $CsGeIBr_2$, and (d) $CsGeBr_3$ in the range from -0.5 eV to 2 eV

The valence band maximum (VBM) is mainly contributed by I 5p and Ge 4s states in $CsGeI_3$ and by I 5p, and Pb 6s states in all three phases of $CsPbI_3$. Whereas the conduction band minimum (CBM) in $CsGeI_3$ is mainly contributed by Ge 4p states, and the CBM in all three phases of $CsPbI_3$ is contributed primarily by Pb 6p. Moreover, it can be observed from Figure 4-21 and Figure 4-22 that the replacement of Pb with Ge leads to narrower bandgaps. Figure 4-21 suggests that the unstable phases of $CsPbI_3$ at room conditions, α-$CsPbI_3$ and γ-$CsPbI_3$, have a close bandgap behavior which is much narrower than the wide bandgap behavior of stable orthorhombic δ-$CsPbI_3$. This agrees with the earlier results we obtained from the band structure calculations. VBM is mainly contributed by Br 4p and Ge 4s in CsGeBr3. In the mixed halide structures, VBM is closely contributed by I 5p, Br 4p, and Ge 4s. The CBM is mainly contributed by Ge 4p states in all the structures of $CsGeI_{3-x}Br_x$. The trend of increasing bandgap with Br content can be observed from Figure 4-22, where the Ge 4p states and halogen p states shift to higher energies in the conduction band. Consequently, the band edge states come mainly from the B-X bonds in all studied materials in this work.

Chapter 5

Conclusions and Future Work

Cesium-based inorganic halide perovskites have been extensively attracting researchers for their exceptional optoelectronic properties and improved stability over organic halide perovskites. Nonetheless, an in-depth understating of their structures, electronic properties, and thermodynamic stability, especially at higher temperatures when phase transformation occurs, was needed. In this work, we used the density functional theory (DFT) in VASP platform and the molecular dynamics (CMD) in LAMMPS to investigate the structural stability, structural properties, electronic properties, and the phase transformation of $CsPbI_3$ from the yellow orthorhombic structure to black cubic structure.

The black cubic $CsPbI_3$ typically undergoes the perovskite phase's instability because the Cs cation is not large enough to hold PbI_6 octahedra. Therefore, it transforms into a non-perovskite counterpart δ-$CsPbI_3$ phase at operational conditions. Quenched orthorhombic γ-$CsPbI_3$ was more stable than α-CsPbI3 at ambient conditions, but it is still less stable than δ-$CsPbI_3$. Our DFT calculations revealed that γ-$CsPbI_3$ is close in its electrical behavior to α-$CsPbI_3$, and they both can be used in theory in photovoltaic applications. In contrast, the stable δ-$CsPbI_3$ has an indirect wide-bandgap which deems it as an insulator.

CMD is used to model the phase transition from δ-$CsPbI_3$ to α-$CsPbI_3$. The choice of the proper forcefield for CMD simulations significantly affects the accuracy of the model outputs. In this work, two forcefields were tested: Buckingham–Coulomb and a newly developed forcefield Hybrid EABC. Buckingham–Coulomb potential fails to reproduce the structure descriptors of $CsPbI_3$ or to predict its phase transition. This might happen because it considers only the pair interactions.

On the other hand, the new Hybrid EABC potential, which combined the embedded atomic method potential with the Buckingham–Coulomb potential, accurately reproduces the main structural and thermodynamics features of $CsPbI_3$. The phase transformation from the orthorhombic to the cubic structure occurred at an average temperature of 594 K with a density change from 5.26 to 4.81 g/cm^3. This matched the experimental results within 1%. Therefore, the Hybrid EABC potential could predict the dynamic interactions among the $CsPbI_3$ constituents and other properties, including thermal conductivity, specific heat, and bulk modulus. This potential could also be utilized to investigate the structural stability and moisture sensitivity and predict the operational temperatures. The results of these investigations will help optimize the experimental work. Finally, the proposed Hybrid EABC potential can be extended to analyze other structures, including the mixed-halides systems of $CsPbI_{3-x}Br_x$.

However, lead's toxicity is one of the bottlenecks limiting the commercialization of high-performance inorganic Cs-based PSCs. Therefore, we extended the investigation to study the structure and electronic properties of the lead-free Ge-based mixed halide family of $CsGeI_{3-x}Br_x$ using DFT in VASP. The structural and electronic properties of $CsGeI_{3-x}Br_x$ (x= 0, 1,2, and 3) have been investigated using DFT. The Generalized Gradient Approximation (GGA) with the PBE and PBEsol exchange-correlation functionals. Both PBE and PBEsol showed relatively similar accuracy when compared to the experimental values of the structural parameters. However, PBE slightly outperformed PBEsol for $CsGeI_{3-x}Br_x$ compounds. Therefore, we decided to use only PBE when we performed the electronic calculations. All structural properties, including the lattice parameter, the volume, and the bond length, decrease with the Br content increase.

Furthermore, the bandgap increases with the increase of the Br content. The electronic density of states revealed that mainly I 5p, Br 4p and Ge 4s states contributed to the VBM whereas, the CBM is mainly contributed by Ge 4p states in all structures of $CsGeI_{3-x}Br_x$. As we established through this work, the average Ge-X bond length decreases while the bandgap increases with

increasing the Br content in $CsGeI_{3-x}Br_x$. This indicates a negative correlation between the Ge-X bond lengths and the energy bandgap. The correlation factor between the energy bandgap and Ge-X bond lengths values obtained by PBE in this work is ~ -95%. This high correlation highlights the importance of obtaining accurate structural parameters before characterizing halide perovskites' electronic properties. These results give insight into designing desirable bandgaps for photovoltaic applications by changing the amount of doping in $CsGeI_{3-x}Br_x$.

Opportunities for Improvement

The DFT results using the PBE functional underestimated the electronic bandgaps. This underestimation results from the fact that the Kohn-Sham energies are not defined by removing or adding electrons. Instead, they are defined as energy states with the bandgap as a difference between the energy of two edge states with the same number of electrons. Additionally, the DFT does not entirely remove the self-interaction error, leading to errors in predicting the electronic properties. The effects of spin and spin coupling were neglected through this work as they require much higher computational costs.

The main limitation of CMD calculations is the simulation time and size. Simulating larger cells would result in more reliable and practical results. However, this requires a much higher computational cost

Future Work

The use of hybrid functionals in DFT gives better bandgap predictions because of the mixing of the Hartree-Fock exchange energies, which provides a better cancelation of self-interaction. HSE06 is a prospective functional that we are currently testing to understand further

and predict the electronic and optical properties, including the refractive index, extinction coefficient, and the absorption of the $CsGeI_{3-x}Br_x$ family.

We plan to use the Hybrid EABC to study the phase transformation of the mixed halide family of $CsPbI_{3-x}Br_x$ and their interaction with moisture (water molecules). Additionally, diffusion and defect densities could also be studied using the Hybrid EABC potential.

References

[1] "Perovskite fever," *Nature Mater,* vol. 13, p. 837, 2014.

[2] A. Kojima, K. Teshima, Y. Shirai and T. Miyasaka, "Organometal halide perovskites as visible-light sensitizers for photovoltaic cells," *Journal of the American Chemical Society,* vol. 131, no. 17, pp. 6050-6051, 2009.

[3] "Best Research-Cell Efficiency Chart," NREL, 2021. [Online]. Available: https://www.nrel.gov/pv/cell-efficiency.html.

[4] S. De Wolf, J. Holovsky, S. Moon, P. Löper, B. Niesen, M. Ledinsky, F. Haug, J. Yum and C. Ballif, "Organometallic halide perovskites: sharp optical absorption edge and its relation to photovoltaic performance," *The journal of physical chemistry letters,* vol. 5, no. 6, pp. 1035-1039, 2014.

[5] T. Baikie, Y. Fang, J. Kadro, M. Schreyer, F. Wei, S. Mhaisalkar, M. Graetzel and T. White, "Synthesis and crystal chemistry of the hybrid perovskite (CH3NH3)PbI3 for solid-state sensitised solar cell applications," *Journal of Materials Chemistry A,* vol. 1, no. 18, pp. 5628-5641, 2013.

[6] N. Park, "Organometal perovskite light absorbers toward a 20% efficiency low-cost solid-state mesoscopic solar cell," *The Journal of Physical Chemistry Letters,* vol. 4, no. 15, pp. 2423-2429, 2013.

[7] S. Kazim, M. Nazeeruddin, M. Grätzel and S. Ahmad, "Perovskite as light harvester: a game changer in photovoltaics," *Angewandte Chemie International Edition,* vol. 53, no. 11, pp. 2812-2824, 2014.

[8] I. Smith, E. Hoke, D. Solis-Ibarra, M. McGehee and H. Karunadasa, "A layered hybrid perovskite solar-cell absorber with enhanced moisture stability," *Angewandte Chemie,* vol. 126, no. 42 , pp. 11414-11417, 2014.

[9] N. Sestu, M. Cadelano, V. Sarritzu, F. Chen, D. Marongiu, R. Piras, M. Mainas, F. Quochi, M. Saba, A. Mura and G. Bongiovanni, "Absorption F-sum rule for the exciton binding energy in methylammonium lead halide perovskites," *The journal of physical chemistry letters,* vol. 6, no. 22, pp. 4566-4572, 2015.

[10] H. S. Kim, S. H. Im and N. G. Park, "Organolead halide perovskite: new horizons in solar cell research," *The Journal of Physical Chemistry C,,* vol. 118, no. 11 , pp. 5615-5625, 2014.

[11] G. E. Eperon, S. D. Stranks, C. Menelaou, M. B. Johnston, L. M. Herz and H. J. Snaith, "Formamidinium lead trihalide: a broadly tunable perovskite for efficient planar heterojunction solar cells," *Energy & Environmental Science,* vol. 7, no. 3 , pp. 982-988, 2014.

[12] C. C. Stoumpos, C. D. Malliakas and M. G. Kanatzidis, "Semiconducting tin and lead iodide perovskites with organic cations: phase transitions, high mobilities, and near-infrared photoluminescent properties," *Inorganic chemistry,* vol. 52, no. 15, pp. 9019-9038 , 2013.

[13] C. Stoumpos, L. Frazer, D. Clark, Y. Kim, S. Rhim, A. Freeman, J. Ketterson, J. Jang and M. Kanatzidis, "Hybrid germanium iodide perovskite semiconductors: active lone pairs, structural distortions, direct and indirect energy gaps, and strong nonlinear optical properties," *Journal of the American Chemical Society,* vol. 137, no. 21, 2015.

[14] N. J. Jeon, J. H. Noh, W. S. Yang, Y. C. Kim, S. Ryu, J. Seo and S. I. Seok, "Compositional engineering of perovskite materials for high-performance solar cells," *Nature,* vol. 517, no. 7535, pp. 476-480, 2015.

[15] Y. Wang, T. Zhang, M. Kan and Y. Zhao, "Bifunctional stabilization of all-inorganic α-CsPbI3 perovskite for 17% efficiency photovoltaics," *Journal of the American Chemical Society,* vol. 140, no. 39, pp. 12345-12348, 2018.

[16] M. Deepa, M. Salado, L. Calio, S. Kazim, S. M. Shivaprasad and S. Ahmad, "Cesium power: low Cs+ levels impart stability to perovskite solar cells," *Physical Chemistry Chemical Physics,* vol. 19, no. 5, pp. 4069-4077, 2017.

[17] M. Kulbak, D. Cahen and G. Hodes, "How important is the organic part of lead halide perovskite photovoltaic cells? Efficient CsPbBr3 cells," *The journal of physical chemistry letters,* vol. 6, no. 13, pp. 2452-2456, 2015.

[18] G. E. Eperon, G. M. Paternò, R. J. Sutton, A. Zampetti, A. A. Haghighirad, F. Cacialli and H. J. Snaith, "Inorganic caesium lead iodide perovskite solar cells," *Journal of Materials Chemistry A,* vol. 3, no. 39, pp. 19688-19695, 2015 .

[19] P. Luo, W. Xia, S. Zhou, L. Sun, J. Cheng, C. Xu and Y. Lu, "Solvent engineering for ambient-air-processed, phase-stable CsPbI3 in perovskite solar cells," *The journal of physical chemistry letters,* vol. 7, no. 18 , pp. 3603-3608, 2016.

[20] T. Zhang, M. I. Dar, G. Li, F. Xu, N. Guo, M. Grätzel and Y. Zhao, "Bication lead iodide 2D perovskite component to stabilize inorganic α-CsPbI3 perovskite phase for high-efficiency solar cells," *Science advances,* vol. 3, no. 9 , p. 1700841, 2017.

[21] D. J. Griffiths and D. F. Schroeter, Introduction to quantum mechanics, Cambridge University Press, 2018.

[22] F. Giustino, Materials modelling using density functional theory: properties and predictions, Oxford University Press, 2014.

[23] J. G. Lee, Computational materials science: an introduction, CRC press, 2016.

[24] C. Kittel, Introduction to solid state physics, Wiley, 1976.

[25] N. W. Ashcroft and N. D. Mermin, Solid state physics, 1976.

[26] D. Hartree, "The Wave Mechanics of an Atom with a Non-Coulomb Central Field. Part II. Some Results and Discussion," *Mathematical Proceedings of the Cambridge Philosophical Society,* vol. 24, no. 1, pp. 111-132, 1928.

[27] V. Fock, "Näherungsmethode zur Lösung des quantenmechanischen Mehrkörperproblems," *Zeitschrift für Physik,* vol. 61, no. (1-2), pp. 126-148, 1930.

[28] D. R. Hartree and W. Hartree, "Self-consistent field, with exchange, for beryllium," *Proceedings of the Royal Society of London. Series A-Mathematical and Physical Sciences,* vol. 150, no. 869 , pp. 9-33, 1935.

[29] P. Hohenberg and W. Kohn, "Inhomogeneous electron gas," *Physical review,* vol. 136, no. 3B, 1964.

[30] W. Kohn and L. J. Sham, "Self-consistent equations including exchange and correlation effects," *Physical review,* vol. 140, no. 4A, 1965.

[31] D. M. Ceperley and B. J. Alder, "Ground state of the electron gas by a stochastic method," *Physical review letters,* vol. 45, no. 7, p. 566, 1980 .

[32] J. P. &. Z. A. Perdew, "Self-interaction correction to density-functional approximations for many-electron systems," *Physical Review B,* vol. 23, no. 10 , p. 5048, 1981 .

[33] J. P. Perdew, J. A. Chevary, S. H. Vosko, K. A. Jackson, M. R. Pederson, D. J. Singh and C. Fiolhais, "Atoms, molecules, solids, and surfaces: Applications of the generalized gradient approximation for exchange and correlation," *Physical review B,* vol. 46, no. 11 , p. 6671, 1992 .

[34] D. C. Langreth and M. J. Mehl, "Beyond the local-density approximation in calculations of ground-state electronic properties," *Physical Review B,* vol. 28, no. 4 , p. 1809, 1983.

[35] J. P. Perdew, K. Burke and M. Ernzerhof, "Generalized gradient approximation made simple," *Physical review letters,* vol. 77, no. 18 , p. 3865, 1996.

[36] J. Perdew, A. Ruzsinszky, G. Csonka, O. Vydrov, G. Scuseria, L. Constantin, X. Zhou and K. Burke, "Restoring the density-gradient expansion for exchange in solids and surfaces," *Physical review letters,* vol. 100, no. 13 , p. 136406, 2008.

[37] H. Hellmann, " Zur Rolle der kinetischen Elektronenenergie für die zwischenatomaren Kräfte," *Zeitschrift für Physik,* vol. 85, no. 3-4, pp. 180-190, 1933.

[38] R. P. Feynman, "Forces in Molecules," *Physical Review,* vol. 56, no. 4, 1939.

[39] L. Verlet, "Computer" experiments" on classical fluids. I. Thermodynamical properties of Lennard-Jones molecules," *Physical review,* vol. 159, no. 1, 1967.

[40] F. Bloch, "Über die quantenmechanik der elektronen in kristallgittern," *Zeitschrift für physik,* vol. 52, no. 7, pp. 555-600, 1929.

[41] D. C. Rapaport and D. C. R. Rapaport, The art of molecular dynamics simulation, Cambridge university press, 2004.

[42] R. Car and M. Parrinello, "Unified Approach for Molecular Dynamics and Density-Functional Theory," 1985.

[43] J. W. Ponder and D. A. Case, "Force fields for protein simulations," vol. 66, 2003.

[44] S. Almishal and O. Rashwan, "New accurate molecular dynamics potential function to model the phase transformation of cesium lead triiodide perovskite (CsPbI3)," *RSC Advances,* vol. 10, no. 72 , pp. 44503-44511, 2020.

[45] J. E. Lennard-Jones, "On the determination of molecular fields. II. From the equation of state of gas," *Proc. Roy. Soc. A ,* vol. 106, pp. 463-477, 1924.

[46] R. A. Buckingham, "The classical equation of state of gaseous helium, neon and argon," *Proceedings of the Royal Society of London. Series A. Mathematical and Physical Sciences,* vol. 168, no. 933, pp. 264-283, 1938.

[47] F. Jensen, Introduction to computational chemistry, John Wiley & sons, 2017.

[48] S. L. Mayo, B. D. Olafson and W. A. Goddard, "DREIDING: a generic force field for molecular simulations," *Journal of Physical chemistry,* vol. 94, no. 26, pp. 8897-8909, 1990.

[49] T. C. Lim, "Alignment of Buckingham parameters to generalized Lennard-Jones potential functions," *Zeitschrift für Naturforschung A ,* vol. 64, no. 3-4, pp. 200-204, 2009.

[50] M. Matsui, "Molecular dynamics study of MgSiO 3 perovskite," *Physics and chemistry of minerals,* vol. 16, no. 3, pp. 234-238, 1988.

[51] M. S. Daw, S. M. Foiles and M. I. Baskes, "The embedded-atom method: a review of theory and applications," *Materials Science Reports,* vol. 9, no. 7-8, pp. 251-310, 1993.

[52] M. S. Daw and M. I. Baskes, "Embedded-atom method: Derivation and application to impurities, surfaces, and other defects in metals," *Physical Review B,* vol. 29, no. 12, p. 6443, 1984.

[53] R. LeSar, Introduction to computational materials science : Fundamentals to applications, 2013.

[54] G. C. Papavassiliou, "Synthetic Three-and Lower-Dimensional Semiconductors Based on Inorganic Units," *Molecular Crystals and Liquid Crystals Science and Technology. Section A,* vol. 286, no. 1, pp. 231-238, 1996.

[55] I. B. Koutselas, L. Ducasse and G. C. Papavassiliou, "Electronic properties of three-and low-dimensional semiconducting materials with Pb halide and Sn halide units," *Journal of Physics: Condensed Matter,* vol. 8, no. 9, 1996.

[56] T. Umebayashi, K. Asai, T. Kondo and A. Nakao, "Electronic structures of lead iodide based low-dimensional crystals," *Physical Review B,* vol. 67, no. 15, 2003.

[57] A. Poglitsch and D. Weber, "Dynamic disorder in methylammoniumtrihalogenoplumbates (II) observed by millimeter-wave spectroscopy," *The Journal of chemical physics,* vol. 87, no. 11 , pp. 6373-6378, 1987.

[58] Y. Wu, F. Xie, H. Chen, X. Yang, H. Su, M. Cai, Z. Zhou, T. Noda and L. Han, "Advanced materials," *Thermally stable MAPbI3 perovskite solar cells with efficiency of 19.19% and area over 1 cm2 achieved by additive engineering,* vol. 29, no. 28 , p. 1701073, 2017.

[59] C. J. Bartel, C. Sutton, B. R. Goldsmith, R. Ouyang, C. B. Musgrave, L. M. Ghiringhelli and M. Scheffler, "New tolerance factor to predict the stability of perovskite oxides and halides," *Science advances,* vol. 5 , no. 2, 2019.

[60] T. Y. T. Song, C. Stoumpos, J. Logsdon, D. Cao, M. Wasielewski, S. Aramaki and M. Kanatzidis, "Importance of reducing vapor atmosphere in the fabrication of tin-based perovskite solar cells," *Journal of the American Chemical Society,* vol. 139, no. 2, pp. 836-842, 2017.

[61] Y. H. Chang, C. H. Park and K. Matsuishi, "First-principles study of the Structural and the electronic properties of the lead-Halide-based inorganic-organic perovskites (CH3NH3) PbX3 and CsPbX3 (X= Cl, Br, I)," *Journal-Korean Physical Society,* vol. 44, pp. 889-893, 2004.

[62] F. Chiarella, A. Zappettini, F. Licci, I. Borriello, G. Cantele, D. Ninno, A. Cassinese and R. Vaglio, "Combined experimental and theoretical investigation of optical, structural, and electronic properties of CH3NH3SnX3 thin films (X= Cl, Br)," *Physical Review B,* vol. 77, no. 4, 2008.

[63] I. Borriello, G. Cantele and D. Ninno, "Ab initio investigation of hybrid organic-inorganic perovskites based on tin halides," *Physical Review B,* vol. 77, no. 23, 2008.

[64] J. Chabot, M. Côté and J. Briere, "Ab initio study of the electronic and structural properties of CsSnI3 perovskite," *In Comptes Rendus Du 17ième Symposium Annuel International Sur Les Systèmes Et Applications Du Calcul de Haute Performance Et Le Symposium OSCAR,* 2003.

[65] L. C. Tang, C. S. Chang and J. Y. Huang, "Electronic structure and optical properties of rhombohedral CsGeI3 crystal," *Journal of Physics: Condensed Matter,* vol. 12, no. 43, 2000.

[66] L. C. Tang, Y. C. Chang, J. Y. Huang, M. H. Lee and C. S. Chang, "First principles calculations of linear and second-order optical responses in rhombohedrally distorted perovskite ternary halides, CsGeX3 (X= Cl, Br, and I)," 2009.

[67] R. Sa, W. Zha, R. Yuan and J. Chen, "Exploring electronic and optical properties of Ge-based perovskites under strain: Insights from the first-principles calculations," *Spectrochimica Acta Part A: Molecular and Biomolecular Spectroscopy,* vol. 229, 2020.

[68] X. Lu, Z. Zhao, K. Li, Z. Han, S. Wei, C. Guo, S. Zhou, Z. Wu, W. Guo and C. Wu, "First-principles insight into the photoelectronic properties of Ge-based perovskites," *RSC advances,* vol. 6, no. 90, 2016.

[69] Y. Gao, Y. Dong, K. Huang, C. Zhang, B. Liu, S. Wang, J. Shi, H. Xie, H. Huang, S. Xiao and J. He, "Highly efficient, solution-processed CsPbI2Br planar heterojunction perovskite solar cells via flash annealing," *ACS Photonics,* vol. 5, no. 10 , p. 41, 2018.

[70] Y. Zhou, J. Chen, O. M. Bakr and H. T. Sun, " Metal-doped lead halide perovskites: synthesis, properties, and optoelectronic applications," *Chemistry of Materials,* vol. 30, no. 19, pp. 6589-6613, 2018.

[71] Z. Yong, S. Guo, J. Ma, J. Zhang, Z. Li, Y. Chen, B. Zhang, Y. Zhou, J. Shu, J. Gu and L. Zheng, "Doping-enhanced short-range order of perovskite nanocrystals for near-unity violet luminescence quantum yield," *Journal of the American Chemical Society,* vol. 140, no. 31, pp. 9942-9951, 2018.

[72] E. Mosconi, A. Amat, M. Nazeeruddin, M. Grätzel and F. De Angelis, "First-principles modeling of mixed halide organometal perovskites for photovoltaic applications," *The Journal of Physical Chemistry C,* vol. 117, no. 27, pp. 13902-13913, 2013.

[73] T. Liashenko, E. Cherotchenko, A. Pushkarev, V. Pakštas, A. Naujokaitis, S. Khubezhov, R. Polozkov, K. Agapev, A. Zakhidov, I. Shelykh and S. Makarov, "Electronic structure of CsPbBr3−xClx perovskites: Synthesis, experimental characterization, and DFT simulations," *Physical Chemistry Chemical Physics,* vol. 21, no. 35, pp. 18930-18938, 2019.

[74] C. Chen, H. Lin, K. Chiang, W. Tsai, Y. Huang, C. Tsao and H. Lin, "All-Vacuum-Deposited Stoichiometrically Balanced Inorganic Cesium Lead Halide Perovskite Solar Cells with Stabilized Efficiency Exceeding 11%," *Advanced materials,* vol. 29, no. 12 , p. 1605290, 2017.

[75] F. Brivio, C. Caetano and A. Walsh, "Thermodynamic origin of photoinstability in the CH3NH3Pb (I1–x Br x) 3 hybrid halide perovskite alloy," *The journal of physical chemistry letters,* vol. 7, no. 6, pp. 1083-1087, 2016.

[76] W. Yin, Y. Yan and S. Wei, "Anomalous alloy properties in mixed halide perovskites," *The journal of physical chemistry letters,* vol. 5, no. 21 , pp. 3625-3631, 2014.

[77] H. Jiang, J. Feng, H. Zhao, G. Li, G. Yin, Y. Han, F. Yan, Z. Liu and S. Liu, "Low temperature fabrication for high performance flexible CsPbI2Br perovskite solar cells," *Advanced Science,* vol. 5, no. 11 , p. 1801117, 2018.

[78] Y. Wang, T. Zhang, F. Xu, Y. Li and Y. Zhao, " A facile low temperature fabrication of high performance CsPbI2Br all-inorganic perovskite solar cells," *Solar Rrl,* vol. 2, no. 1, p. 1700180, 2018.

[79] J. Zhang, Z. Jin, L. Liang, H. Wang, D. Bai, H. Bian, K. Wang, Q. Wang, N. Yuan, J. Ding and S. Liu, " Iodine-Optimized Interface for Inorganic CsPbI2Br Perovskite Solar Cell to

Attain High Stabilized Efficiency Exceeding 14%," *Advanced Science,* vol. 5, no. 12, p. 1801123, 2018.

[80] L. Yan, Q. Xue, M. Liu, Z. Zhu, J. Tian, Z. Li, Z. Chen, Z. Chen, H. Yan, H. Yip and Y. Cao, "Interface engineering for all-inorganic CsPbI2Br perovskite solar cells with efficiency over 14%," *Advanced materials,* vol. 30, no. 33 , p. 1802509, 2018.

[81] D. Bai, H. Bian, Z. Jin, H. Wang, L. Meng, Q. Wang and S. Liu, "Temperature-assisted crystallization for inorganic CsPbI2Br perovskite solar cells to attain high stabilized efficiency 14.81%," *Nano energy,* vol. 52 , pp. 408-415, 2018.

[82] S. Pramchu, A. Jaroenjittichai and Y. Laosiritaworn, "Effects of bromine substitution for iodine on structural stability and phase transition of CsPbI3," *Applied Surface Science,* vol. 496 , p. 143593, 2019.

[83] E. Mosconi, P. Umari and F. De Angelis, "Electronic and optical properties of mixed Sn–Pb organohalide perovskites: a first principles investigation," *Journal of Materials Chemistry A,* vol. 3, no. 17, pp. 9208-9215, 2015.

[84] G. T. Wang, J. H. Wei and Y. F. Peng, "Electronic and optical properties of mixed perovskites CsSnxPb (1− x)I3," *AIP Advances,* vol. 6, no. 6, p. 065213, 2016.

[85] S. Zhu, J. Ye, Y. Zhao and Y. Qiu, "Structural, Electronic, Stability, and Optical Properties of CsPb1–x Sn x IBr2 Perovskites: A First-Principles Investigation," *The Journal of Physical Chemistry C,* vol. 123, no. 33 , pp. 20476-20487, 2019.

[86] N. Li, Z. Zhu, J. Li, A. Jen and L. Wang, "Inorganic CsPb1− xSnxIBr2 for Efficient Wide-Bandgap Perovskite Solar Cells," *Advanced energy materials,* vol. 8, no. 22, p. 1800525, 2018.

[87] J. Liang, P. Zhao, C. Wang, Y. Wang, Y. Hu, G. Zhu, L. Ma, J. Liu and Z. Jin, "CsPb0. 9Sn0.1IBr2 based all-inorganic perovskite solar cells with exceptional efficiency and stability," *Journal of the American Chemical Society,* vol. 139, no. 40, p. 140, 2017.

[88] R. Mayengbam, S. Tripathy and G. Palai, " First-Principle Insights of Electronic and Optical Properties of Cubic Organic–Inorganic MAGe x Pb (1–x) I3 Perovskites for Photovoltaic Applications," *The Journal of Physical Chemistry C,* vol. 122, no. 49, 2018.

[89] P. Sun, Q. Li, S. Feng and Z. Li, "Mixed Ge/Pb perovskite light absorbers with an ascendant efficiency explored from theoretical view," *Physical Chemistry Chemical Physics,* vol. 18, no. 21 , pp. 14408-14418, 2016.

[90] Y. Liang, L. Guan, X. Xu, S. Han, J. Guo, J. Wang, X. Chen, Z. Zhang and X. Li, "Effects of the Dopant Site on the Absorption Properties of CsPb1–x M x I2Br (M= Ge, Sn, Sr, and Cu): A First-Principles Investigation," *The Journal of Physical Chemistry C,* vol. 124, no. 11, pp. 6028-6037, 2020.

[91] F. Yang, D. Hirotani, G. Kapil, M. Kamarudin, C. Ng, Y. Zhang, Q. Shen and S. Hayase, "All-Inorganic CsPb1−xGexI2Br Perovskite with Enhanced Phase Stability and Photovoltaic Performance," *Angewandte chemie international edition,* vol. 57, no. 39, 2018.

[92] M. Chen, M. Ju, H. Garces, A. Carl, L. Ono, Z. Hawash, Y. Zhang, T. Shen, Y. Qi, R. Grimm and D. Pacifici, "Highly stable and efficient all-inorganic lead-free perovskite solar cells with native-oxide passivation," *Nature communications* , vol. 10, no. 1, pp. 1-8, 2019.

[93] J. Chen and J. D. Lee, "The Buckingham Catastrophe in multiscale modelling of fracture," 2011.

[94] E. Fransson and J. L. Hakansson, "Local and Global Ordering in Barium Zirconate, a Model Potential Study," 2014.

[95] J. A. Souza and J. P. Rino, "A molecular dynamics study of structural and dynamical correlations of CaTiO3," 2011.

[96] A. Mattoni, A. Filippetti and C. Caddeo, "Modeling hybrid perovskites by molecular dynamics," 2016.

[97] A. Mattoni, A. Filippetti, M. I. Saba and P. Delugas, "Methylammonium rotational dynamics in lead halide perovskite by classical molecular dynamics: the role of temperature," 2015 .

[98] S. Maheshwari, M. B. Fridriksson, S. Seal, J. Meyer and F. C. Grozema, "The Relation between Rotational Dynamics of the Organic Cation and Phase Transitions in Hybrid Halide Perovskites," *The Journal of Physical Chemistry C* , vol. 123, no. 23, pp. 14652-14661, 2019.

[99] P. Delugas, C. Caddeo, A. Filippetti and A. Mattoni, "Thermally activated point defect diffusion in methylammonium lead trihalide: anisotropic and ultrahigh mobility of iodine," *The journal of physical chemistry letters,* vol. 7 , no. 13, pp. 2356-2361, 2016.

[100] J. Wang, L. Zhao, M. Wang and S. Lin, "Molecular Insights into Early Nuclei and Interfacial Mismatch during Vapor Deposition of Hybrid Perovskites on Titanium Dioxide Substrate," *Crystal Growth & Design,* vol. 17, no. 12, pp. 6201-6211, 2017.

[101] C. Wang, Y. Liu, S. F. Liu, B. Li and Y. Chen, "Giant phonon tuning effect via pressure-manipulated polar rotation in perovskite MAPbI3," *The journal of physical chemistry letters,* vol. 9, no. 11, pp. 3029-3034, 2018.

[102] J. Ma and L. W. Wang, "The nature of electron mobility in hybrid perovskite CH3NH3PbI3," *Nano letters, 17(6), 3646-3654,* 2017.

[103] C. G. Bischak, A. B. Wong, E. Lin, D. T. Limmer, P. Yang and N. S. Ginsberg, "Tunable polaron distortions control the extent of halide demixing in lead halide perovskites," *The journal of physical chemistry letters, 9(14), 3998-4005,* 2018.

[104] A. Mattoni and C. Caddeo, "Dielectric function of hybrid perovskites at finite temperature investigated by classical molecular dynamics," *The Journal of Chemical Physics, 152(10), 104705.,* 2020.

[105] A. Giri, A. Chen, A. Mattoni, K. Aryana, D. Zhang, H. X, S. Lee, J. Choi and P. Hopkins, "Ultralow thermal conductivity of two-dimensional metal halide perovskites," *Nano Letters 20, 5, 3331–3337,* 2020.

[106] T. Hata, G. Giorgi, K. Yamashita, C. Caddeo and A. & Mattoni, "Development of a classical interatomic potential for MAPbBr3," 2017.

[107] C. Caddeo, M. I. Saba, S. Meloni, A. Filippetti and A. Mattoni, "Collective molecular mechanisms in the CH3NH3PbI3 dissolution by liquid water," *ACS nano, 11(9), 9183-9190,* 2017.

[108] C. Caddeo, D. Marongiu, S. Meloni, A. Filippetti, F. Quochi, M. Saba and A. Mattoni, "Hydrophilicity and Water Contact Angle on Methylammonium Lead Iodide," Vols. Advanced Materials Interfaces, 6(3), 1801173, 2019.

[109] H. C. M. and F. C. L., "A new potential for methylammonium lead iodide," *Physical Chemistry Chemical Physics* , vol. 19, no. 3, pp. 2313-2321, 2017.

[110] H. A. Chen and C. W. Pao, "Fast and Accurate Artificial Neural Network Potential Model for MAPbI3 Perovskite Materials," *ACS omega,* vol. 4, no. 6, pp. 10950-10959, 2019.

[111] E. I. Marchenko, S. A. Fateev, A. A. Petrov, E. A. Goodilin, N. N. Eremin and A. B. Tarasov, "Transferable Approach of Semi-Empirical Modeling of Disordered Mixed-Halide Hybrid Perovskites CH3NH3Pb (I1–x Br x) 3: Prediction of Thermodynamic Properties, Phase Stability, and Deviations from Vegard's Law," *The Journal of Physical Chemistry C, 123(42),* 2019.

[112] D. L. Busipalli, K. Y. Lin, S. Nachimuthu and J. C. Jiang, "Enhanced moisture stability of cesium lead iodide perovskite solar cells–a first-principles molecular dynamics study," 2020 .

[113] B. Wang, N. Novendra and A. Navrotsky, "Energetics, structures, and phase transitions of cubic and orthorhombic cesium lead iodide (CsPbI3) polymorphs," *Journal of the American Chemical Society,* vol. 141, no. 37, pp. 14501-14504, 2019.

[114] S. R. G. Balestra, J. M. Vicent-Luna, S. Calero, S. Tao and J. A. Anta, "Efficient Modelling of Ion Structure and Dynamics in Inorganic Metal Halide Perovskites," 2020.

[115] G. Kresse and J. Furthmüller, "Efficient iterative schemes forab initiototal-energy calculations using a plane-wave basis set," *Physical Review B,* vol. 54, no. 16, pp. 11169-11186, 1996.

[116] G. Kresse, Joubert and D., "From ultrasoft pseudopotentials to the projector augmented-wave method," *Physical Review B,* vol. 59, no. 3, pp. 1758-1775, 1999.

[117] E. H. Lieb and S. Oxford, "Improved lower bound on the indirect Coulomb energy," *International Journal of Quantum Chemistry,* vol. 19 , no. 3, pp. 427-439, 1981.

[118] R. Armiento and A. Mattsson, "Functional designed to include surface effects in self-consistent density functional theory," *Physical Review B,* vol. 72, no. 8 , p. 085108, 2005.

[119] D. Rappoport, N. Crawford, F. Furche and K. Burke, "Approximate density functionals: which should I choose?," in *Encyclopedia of Inorganic and Bioinorganic Chemistry*, 2011.

[120] L. Pedroza, A. da Silva and K. Capelle, "Gradient-dependent density functionals of the Perdew-Burke-Ernzerhof type for atoms, molecules, and solids," *Physical Review B,* vol. 79, no. 20, p. 201106, 2009.

[121] L. He, F. Liu, G. Hautier, M. Oliveira, M. Marques, F. Vila, J. Rehr, G. Rignanese and A. Zhou, "Accuracy of generalized gradient approximation functionals for density-functional perturbation theory calculations," *Physical Review B,* 2014.

[122] G. Csonka, J. Perdew, A. Ruzsinszky, P. Philipsen, S. Lebègue, J. Paier, O. Vydrov and J. Ángyán, "Assessing the performance of recent density functionals for bulk solids," *Physical Review B,* vol. 79, no. 10, 2009.

[123] S. Shastri and S. Pandey, "A comparative study of different exchange-correlation functionals in understanding structural, electronic and thermoelectric properties of Fe2VAl and Fe2TiSn compounds," *Computational Materials Science,* vol. 143 , pp. 316-324, 2018.

[124] P. Borlido, T. Aull, A. Huran, F. Tran, M. Marques and S. Botti, "Large-scale benchmark of exchange–correlation functionals for the determination of electronic band gaps of solids," *Journal of chemical theory and computation,* vol. 15, no. 9, 2019.

[125] N. Hernandez-Haro, J. Ortega-Castro, Y. B. Martynov, R. G. Nazmitdinov and A. Frontera, "DFT prediction of band gap in organic-inorganic metal halide perovskites: An exchange-correlation functional benchmark study," *Chemical Physics,* vol. 516, pp. 225-231, 2019.

[126] P. E. Blöchl, O. Jepsen and O. K. Andersen, " Improved tetrahedron method for Brillouin-zone integrations," *Physical Review B,* vol. 49, no. 23 , p. 16223, 1994.

[127] C. L. Fu and K. M. Ho, "First-principles calculation of the equilibrium ground-state properties of transition metals: Applications to Nb and Mo," *Physical Review B,* vol. 28, no. 10, p. 5480, 1983.

[128] K. Momma and F. Izumi, "VESTA 3 for three-dimensional visualization of crystal, volumetric and morphology data," *J. Appl. Crystallogr., 44, 1272-1276* , 2011.

[129] V. Wang, N. Xu, J. Liu, G. Tang and W. Geng, "VASPKIT: a user-friendly interface facilitating high-throughput computing and analysis using VASP code," *arXiv:1908.08269,* 2019.

[130] S. Plimpton, "Fast Parallel Algorithms for Short-Range Molecular Dynamics," 1995.

[131] M. J. L. Sangster and R. M. Atwood, "Interionic potentials for alkali halides. II. Completely crystal independent specification of Born-Mayer potentials," *Journal of Physics C: Solid State Physics,* vol. 11, no. 8 , p. 1541, 1978.

[132] K. Mirskaya, "Combining rules for interatomic potential functions of Buckingham form," 1973.

[133] A. Nichol and G. Ackland, "Property trends in simple metals: An empirical potential approach," *Physical Review B, 93(18), 184101. DOI: 10.1103/physrevb.93.184101,* 2016.

[134] K. Wang, W. Zhu, M. Xiang, Y. Xu, G. Li and J. Chen, "Improved embedded-atom model potentials of Pb at high pressure: application to investigations of plasticity and phase transition under extreme conditions," *Modelling and Simulation in Materials Science and Engineering, 27(1), 015001,* 2018.

[135] P. Hirel, "Atomsk: A tool for manipulating and converting atomic data files," *Computer Physics Communications, 197, 212–219,* 2015.

[136] S. Nosé, "A unified formulation of the constant temperature molecular dynamics methods.," *The Journal of chemical physics, 81(1), 511-519,* 1984.

[137] A. Stukowski, "Visualization and analysis of atomistic simulation data with OVITO–the Open Visualization Tool," *Modelling and Simulation in Materials Science and Engineering, 18(1), 015012,* 2009.

[138] R. Sutton, M. Filip, A. Haghighirad, N. Sakai, B. Wenger, F. Giustino and H. Snaith, "Cubic or Orthorhombic? Revealing the Crystal Structure of Metastable Black-Phase CsPbI3 by Theory and Experiment," *ACS Energy Letters,* vol. 3, no. 8, pp. 1787-1794, 2018.

[139] Q. A. Akkerman, V. D'Innocenzo, S. Accornero, A. Scarpellini, A. Petrozza, M. Prato and L. Manna, "Tuning the optical properties of cesium lead halide perovskite nanocrystals by anion exchange reactions," *Journal of the American Chemical Society,* vol. 137, no. 32 , pp. 10276-10281, 2015.

[140] D. M. Trots and S. V. Myagkota, "High-temperature structural evolution of caesium and rubidium triiodoplumbates," *Journal of Physics and Chemistry of Solids,* vol. 69, no. 10, pp. 2520-2526, 2008.

[141] Z. Lin, L. Tang and C. Chou, "Study on mid-IR NLO crystals CsGe(BrxCl1−x)3," *Optical Materials,* vol. 31, no. 1, pp. 28-34, 2008.

[142] D. B. Straus, S. Guo, M. Abeykoon and R. J. & Cava, "Understanding the Instability of the Halide Perovskite CsPbI3 through Temperature-Dependent Structural Analysis," *Advanced Materials,* vol. 32, no. 32, 2020.

[143] H. Fujiwara and R. W. Collins, Spectroscopic Ellipsometry for Photovoltaics, Switzerland: Springer, 2018.

[144] S. Sharma, N. Weiden and A. Weiss, "Phase diagrams of quasibinary systems of the type: ABX3—A′ BX3; ABX3—AB′ X3, and ABX3—ABX′ 3; X= halogen," *Zeitschrift für Physikalische Chemie* , vol. 175, no. 1, pp. 63-80, 1992.

[145] J. P. Perdew, "Density functional theory and the band gap problem," *International Journal of Quantum Chemistry*, vol. 28, no. S19, pp. 497-523, 1985 .

[146] G. Murtaza and I. Ahmad, "First principle study of the structural and optoelectronic properties of cubic perovskites CsPbM3 (M= Cl, Br, I)," *Physica B: Condensed Matter*, vol. 406, no. 17 , pp. 3222-3229, 2011.

[147] Z. Yang, A. Surrente, K. Galkowski, A. Miyata, O. Portugall, R. Sutton, A. Haghighirad, H. Snaith, D. Maude, P. Plochocka and R. Nicholas, "Impact of the halide cage on the electronic properties of fully inorganic cesium lead halide perovskites," *ACS Energy Letters*, vol. 2, no. 7 , pp. 1621-1627, 2017.

[148] G. Walters and E. Sargent, "Electro-optic response in germanium halide perovskites," *The journal of physical chemistry letters*, vol. 9, no. 5 , pp. 1018-1027, 2018.

[149] M. Roknuzzaman, K. K. Ostrikov, H. Wang, A. Du and T. Tesfamichael, "Towards lead-free perovskite photovoltaics and optoelectronics by ab-initio simulations," *Scientific reports*, vol. 7, no. 1, pp. 1-8, 2017.

[150] T. Krishnamoorthy, H. Ding, C. Yan, W. Leong, T. Baikie, Z. Zhang, M. Sherburne, S. Li, M. Asta, N. Mathews and S. Mhaisalkar, "Lead-free germanium iodide perovskite materials for photovoltaic applications," *Journal of Materials Chemistry A*, vol. 3, no. 47, pp. 23829-23832, 2015.